



# Causal features in turbulent channel flow

Kosuke Osawa<sup>1,†</sup> and Javier Jiménez<sup>1</sup>

<sup>1</sup>School of Aeronautics, Universidad Politécnica de Madrid, 28040 Madrid, Spain

(Received 24 May 2024; revised 5 August 2024; accepted 29 August 2024)

The causal relevance of local flow conditions in open-channel turbulence is analysed using ensembles of interventional experiments in which the effect of perturbing the flow within a small cell is monitored at some future time. When this is done using the relative amplification of the perturbation energy, causality depends on the flow conditions within the cell before it is perturbed, and can be used as a probe of the flow dynamics. The key scaling parameter is the ambient shear, which is also the dominant diagnostic variable for wall-attached perturbations. Away from the wall, the relevant variables are the streamwise and wall-normal velocities. Causally significant cells are associated with sweeps that carry the perturbation towards the stronger shear near the wall, whereas irrelevant ones are associated with ejections that carry it towards the weaker shear in the outer layers. Causally significant and irrelevant cells are themselves organised into structures that share many characteristics with classical sweeps and ejections, such as forming spanwise pairs whose dimensions and geometry are similar to those of classical quadrants. At the wall, this is consistent with causally significant configurations in which a high-speed streak overtakes a low-speed one, and causally irrelevant ones in which the two streaks pull apart from each other. It is argued that this is probably associated with streak meandering.

**Key words:** turbulent boundary layers, turbulence theory, computational methods

## 1. Introduction

Although turbulence is a high-dimensional chaotic system, it is often modelled as a collection of compact and approximately autonomous coherent structures. These are typically intermittent, emerging and vanishing with a lifetime and frequency that depend on their nature and size, and are characterised both by evolving relatively independently from their flow environment, and by having a measurable influence on the rest of the flow (Jiménez 2018*a*). As such, it is important to clarify not only how they behave individually, but how are they connected among themselves in space and in time.

† Email address for correspondence: [kosawa@torroja.dmt.upm.es](mailto:kosawa@torroja.dmt.upm.es)

Such causal connections would help us to understand how turbulence works, both from the fundamental point view and in practical applications connected with flow control and prediction. For example, it is important to avoid introducing in the initial conditions of numerical weather forecasting spurious perturbations that would later amplify significantly (Rodwell & Wernli 2023), and identifying such highly influential events would help us to improve prediction accuracy. Another example is flow control, which intrinsically tries to modify the future of the flow by altering its present state. Understanding which structures are causally important and which have no significant effect in the evolution of the flow would clearly help in optimising this process.

Conversely, elucidating the connections between different flow regions, not necessarily initially identified as coherent, may lead to the discovery of novel coherent structures that describe turbulence better than the known ones, or to previously overlooked connections between known structures that can be incorporated into better flow models (Jiménez 2020*b*; Jiménez 2023).

For example, quasi-streamwise rollers, streamwise-velocity streaks and wall-normal velocity bursts are believed to be essential for maintaining wall-bounded turbulence. The most common hypothesis is that there is a self-sustaining process (SSP) in which at least two of these structures mutually induce each other (Jiménez & Moin 1991; Hamilton, Kim & Waleffe 1995; Waleffe 1997), but the details are incomplete. For example, recent evidence suggests that bursts are able to sustain a cycle by themselves (Jiménez 2018*a*), while streaks are byproducts rather than actors in the SSP (Jiménez 2022). Even apparently straightforward connections, such as the generation of the streaks by bursts (Kim, Kline & Reynolds 1971), are only incompletely understood, because the two phenomena have very different length scales (Jiménez 2018*a*). Establishing the causality relations between these different structures would throw light on whether they are indeed connected, on the sequence in which they are linked, and on whether some component is missing from the model.

With the goal of minimising bias, our strategy is to exclusively characterise flow regions in terms of their influence on the future of the flow, without necessarily relating them to previously known coherent structures. Only once a particular flow template has been identified as highly causal or as especially irrelevant will we try to classify it within existing theories, or to recognise it as something new.

There are two general approaches to causality. The first is observational and non-intrusive, and is often the only option when the system is hard to replicate (e.g. astrophysics), difficult to experiment with (e.g. some social sciences), or simply too large to simulate easily. Unfortunately, it is generally believed that observation is not enough to unambiguously establish cause and effect, because correlation does not imply causation (Granger 1969; Pearl 2009), but even in those cases, a careful consideration of the temporal evolution of the system may lead to the identification of causal histories when they cross neighbourhoods of particular interest, typically extreme events (Angrist, Imbens & Rubin 1996). A related approach is the operator representation of turbulence time series, examples of which are Froyland & Padberg (2009), Kaiser *et al.* (2014), Schmid, García-Gutiérrez & Jiménez (2018), Brunton, Noack & Koumoutsakos (2020), Fernex, Noack & Semaan (2021), Taira & Nair (2022), Jiménez (2023) and Souza (2023), among others. Another example is the analysis of data series from wall-bounded turbulence by Lozano-Durán, Bae & Encinar (2020) using tools of transfer entropy, or the improved version in which their applicability to subgrid modelling and flow control was demonstrated by Lozano-Durán & Arranz (2022).

The alternative is interventional causality, in which the system is modified directly and the consequences observed. This offers more control over what is being analysed, and safer

inferences (Pearl 2009), but presumes a sufficiently cheap way of modifying the system. Essentially, in dynamical system notation, non-interventional methods provide information about the behaviour of the system while it moves within its attractor, while interventional ones give additional information about the system by observing what happens outside it.

Turbulence, which is expensive to simulate and hard to modify experimentally, was for a long time considered to be in the group of phenomena that could be only observed, but the increased speed of computers, as well as better experimental techniques, slowly eroded that difficulty (Jiménez & Moin 1991; Jiménez & Pinelli 1999). More recently, fast graphics processing units (GPUs) speeded up the numerical simulation of realistic turbulent flows to the point of allowing the practical simulation of artificially modified flow ensembles that can be considered interventional (Vela-Martín & Jiménez 2021). They have opened the possibility of Monte Carlo studies in which the consequences of ‘randomly’ modified flows are examined.

Examples of this approach are Jiménez (2018*b*, 2020*b*), who introduced localised perturbations in two-dimensional turbulence in order to determine which parts of the flow result in significant perturbation growth or decay after a certain time. This allowed the identification of causally significant and irrelevant flow structures, including the relatively unexpected relevance of vortex dipoles rather than individual vortices, and eventually led to new models for the two-dimensional energy cascade (Jiménez 2021). Encinar & Jiménez (2023) extended the technique to three-dimensional homogeneous isotropic turbulence, and demonstrated that causal events are in that case characterised by either high kinetic energy or high dissipation rate, depending on the spatial scale of the initial perturbation, and that strong strain, rather than high vorticity, is the main prerequisite for perturbation growth. In these two cases, it is interesting that some of the significant structures were not the classically expected ones, underlining the ability of Monte Carlo interventional experiments to mitigate the bias of conventional wisdom.

In this study, we adopt the interventional approach, following the basic methodology in Jiménez (2018*b*). Spatially localised perturbations are imposed on a fully developed turbulent channel flow, and their influence is measured by their ability to alter the future evolution of the flow.

Numerical experiments that track the development of perturbation ensembles in wall turbulence are not new, probably starting with the computation by Keefe, Moin & Kim (1992) of the Lyapunov spectrum in a low-Reynolds-number channel. On a similar subject, Nikitin (2008, 2018) investigated the Reynolds number scaling of the leading Lyapunov exponent of a turbulent channel. Lyapunov analysis does not typically control the form of the initial perturbation, leaving the system to choose the most unstable direction in state space, and taking precautions to avoid nonlinearities, but Cherubini *et al.* (2010) and Farano *et al.* (2017) turned the problem around by searching for weakly or fully nonlinear perturbations that optimally grow in energy after a given target time. They worked on an initially stationary flow with a turbulent profile, and when they constrain the initial energy of the perturbation, they obtain optimals that are localised in physical space. More recently, Ciola *et al.* (2023) extended the analysis to snapshots of real turbulence, finding that for properly chosen target times, the optimal precursor is an early stage of an Orr burst. However, due to the difficulty of convergence over long times, their results apply only to short delays of the order of a few tens of viscous units. Moreover, the solution is optimal only for the snapshot at which it is applied, making it difficult to generalise the result.

The choice of the size of the initial perturbations is important, and data assimilation experiments have been conducted to estimate the minimum size below which perturbations are enslaved to their environment. The first was probably by Yoshida, Yamaguchi &

Kaneda (2005) in isotropic three-dimensional turbulence, who showed that randomised scales smaller than 30 Kolmogorov viscous lengths (Kolmogorov 1941) are regenerated if continuously assimilated to larger structures. Wang & Zaki (2022) conducted similar experiments in channel turbulence. They replaced some layers with white noise, and showed how they synchronised with the original flow when assimilated through their boundaries. The maximum synchronisation thickness is approximately 30 viscous lengths (approximately 12 Kolmogorov units) for layers attached to the wall, and twice the Taylor microscale for layers away from it. However, since Encinar & Jiménez (2023) found that freely evolving perturbations grow even below the assimilation limit, the result in wall-bounded turbulence remains uncertain.

The present study targets the nonlinear evolution of localised perturbations applied to instantaneous snapshots of turbulent channels at a moderate but non-trivial Reynolds number, over times of the order of an eddy turnover. A Monte Carlo search is used to apply the analysis across snapshots, and across as many combinations of perturbation location, size and target time as is practicable. The basic assumption is that causality depends of the local state of the neighbourhood at which the perturbation is applied, and the details of this dependence are extracted from the database of numerical experiments using standard methods of data analysis.

The organisation of the paper is as follows. The numerical set-up and the definition of the initial perturbations are described in § 2. How their evolution can be used to determine causality is discussed in §§ 3 and 4, and the relation between causal structures and the surrounding flow field is discussed in § 5. Conclusions are offered in § 6.

## 2. Numerical set-up

To save computational resources, we analyse simulations of a pressure-driven turbulent open channel flow in a doubly periodic domain, between a no-slip wall at  $y = 0$  and an impermeable free-slip wall at  $y = h$ . The streamwise, wall-normal and spanwise directions are  $x$ ,  $y$  and  $z$ , respectively, and the corresponding velocities are  $u$ ,  $v$  and  $w$ , although position and velocities are occasionally denoted by their components  $\boldsymbol{x} = \{x_j, j = 1, 2, 3\}$ . The domain size is  $L_x \times L_y \times L_z = \pi h \times h \times \pi h$ , and the Reynolds number is  $Re_\tau = u_\tau h / \nu = 600.9$ . The ‘+’ superscript denotes wall units, normalised with the friction velocity  $u_\tau$  and with the kinematic viscosity  $\nu$ . Capital letters, as in  $U(y)$ , denote variables averaged over the simulation ensemble and over wall-parallel planes; lowercase letters are fluctuations with respect to this average, and primes are root-mean-square fluctuation intensities. Repeated indices, including squares, imply summations unless noted otherwise. The simulation code is standard dealiased Fourier spectral along  $x$  and  $z$ , as in Kim, Moin & Moser (1987), but uses seven-points-stencil compact finite differences for the wall-normal derivatives, as in Hoyas & Jiménez (2006). Time marching is semi-implicit third-order Runge–Kutta (Spalart, Moser & Rogers 1991), and the mass flux is kept constant. The numerical  $y$  grid is stretched at the no-slip wall with a hyperbolic tangent. See table 1 for other numerical parameters.

Figure 1(a) compares the resulting fluctuation profiles with existing data from regular and open channels. It was shown by Lozano-Durán & Jiménez (2014a) that a computational box with  $L_z/h = \pi$  reproduces well the statistics of regular channels, and figure 1 shows that the same is true for open ones. In particular, figure 1(b) shows that the spanwise kinetic energy spectrum fits well within the computational box. On the other hand, the figure shows that open and full channels agree only below  $y/h \approx 0.5$ , above which the effect of ‘splating’ at the top wall is particularly visible in the fluctuations of the cross-flow velocities (Perot & Moin 1995). We will use only the range  $y^+ \lesssim 300$  for

$U_b h / \nu$	$Re_\tau$	$L_x \times L_y \times L_z$	$N_x \times N_y \times N_z$	$\Delta x^+$	$\Delta y_{min}^+$	$\Delta y_{max}^+$	$\Delta z^+$
11 180	600.9	$\pi h \times h \times \pi h$	$128 \times 192 \times 256$	14.7	0.46	6.51	7.4

Table 1. Computational parameters:  $L_i$  is the domain size along the  $i$ th direction,  $h$  is the ‘half-channel’ height, equivalent to the domain height in open channels, and  $U_b$  is the bulk velocity. The grid dimensions  $N_i$  and effective resolutions  $\Delta x_i$  are expressed in terms of Fourier modes.

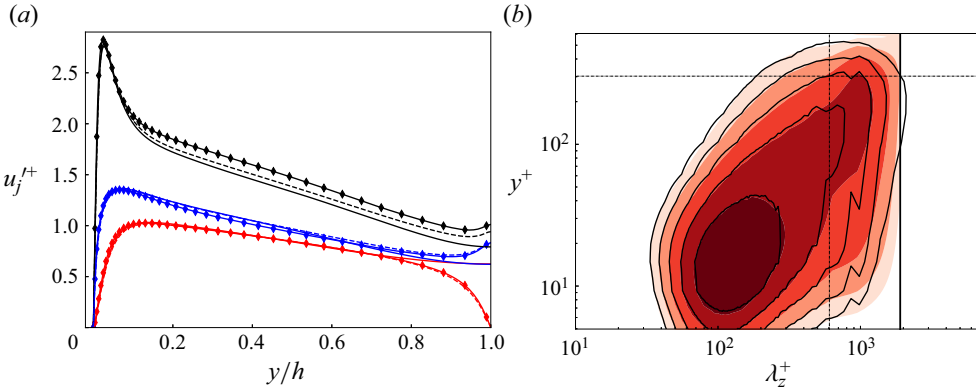


Figure 1. (a) Velocity fluctuation intensities. Symbols represent the open channel at  $Re_\tau = 601$ ; dashed lines represent the open channel at  $Re_\tau = 541$  (Pirozzoli 2023); and solid lines represent the full channel at  $Re_\tau = 547$  (del Álamo & Jiménez 2003). Black indicates  $u'$ , red indicates  $v'$ , and blue indicates  $w'$ . (b) Premultiplied spanwise spectrum of the turbulent kinetic energy, normalised with  $u_\tau^2$ . Contours are logarithmically equispaced from  $k_z E_{KK} / u_\tau^2 = 0.56$ –2.8. The heavier vertical line is the present computational box. The thinner vertical line is  $\lambda_z = 2\pi/k_z = h$ , and the horizontal line is  $y^+ = 300$ . Filled contours are the present simulation; lines are from del Álamo & Jiménez (2003).

the rest of the paper. It is also clear from the figure that the energy at long wavelengths above  $y^+ = 100$  is higher than in del Álamo & Jiménez (2003). This is due to the short computational box, which inhibits the instability of the streaks (Abe, Antonia & Toh 2018), and results in two pairs of large streamwise streaks and rollers that dominate the flow.

The original code was ported to CUDA by Vela-Martín *et al.* (2021) for the efficient simulation of high-Reynolds number channel turbulence on GPU clusters. It has been adapted to a single GPU for the present experiments, but the original reference should be consulted for full details.

### 2.1. The initial perturbations

As mentioned in the Introduction, the interventional identification of causality follows (Jiménez 2018b, 2020b). The idea is to apply a spatially localised initial perturbation to existing turbulence, after which the flow is allowed to develop freely (see figure 2). The effect is measured after some time. Unlike the sensitivity analysis of the mean velocity profile in Farano *et al.* (2017), each causality experiment is the response to a particular perturbation on a particular location of a given flow snapshot, and the numerical experiment has to be repeated many times for different snapshots and perturbations. The goal is to create a database of responses from which to extract the characteristics that make a particular flow location influential for the future behaviour of turbulence (i.e.

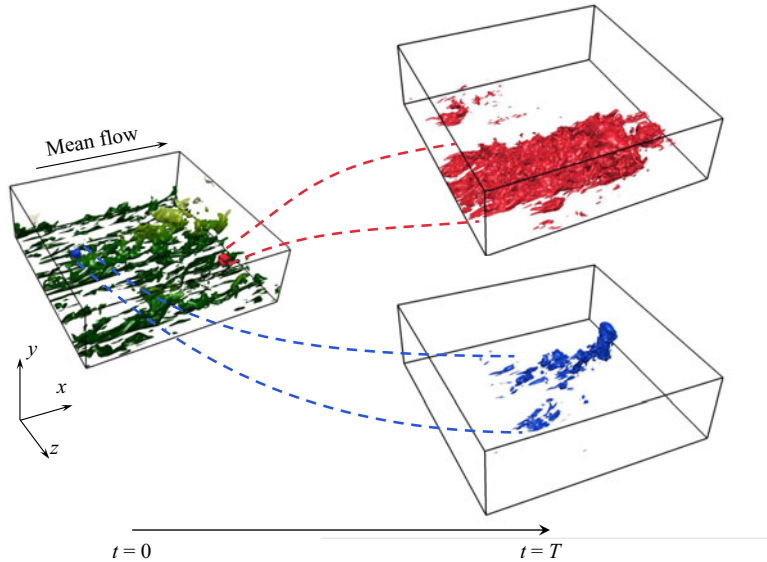


Figure 2. Schematic of the numerical experiment. Green represents the isosurface of the turbulent kinetic energy for the reference flow at  $t = 0$ ,  $|\mathbf{u}_{ref}|^+ = 4.5$ . Colour intensity encodes the distance from the wall. Red represents the perturbation kinetic energy at some later time,  $|\mathbf{u}_{ref}(T) - \mathbf{u}_{mod}(T)|^+ = 0.17$ , for a causally significant perturbation. Blue represents the same for a causally irrelevant perturbation.

causally significant). To ensure independence, the 40 initial reference snapshots used for our experiments are separated by at least 1.4 turnovers (defined as  $h/u_\tau$ ).

Perturbations modify the flow within a cubical cell of side  $l_{cell}$  centred at  $\mathbf{x}_c$ . Although there are countless choices for the form of the disturbance, and even if experience shows that the manner in which the flow is disturbed influences the outcome of the experiment (Jiménez 2020b; Encinar & Jiménez 2023), cost considerations limit us to a single perturbation scheme. Specifically, the flow is modified by removing the velocity fluctuations within the cell, overwriting the velocity field with its  $y$ -dependent cell average. Defining the  $y$ -dependent cell average of a variable  $f$  as

$$\bar{f}^c(y) = l_{cell}^{-2} \int_{x_c - l_{cell}/2}^{x_c + l_{cell}/2} \int_{z_c - l_{cell}/2}^{z_c + l_{cell}/2} f(x, y, z) \, dx \, dz, \quad (2.1)$$

the perturbed velocity  $\mathbf{u}_{mod}$  is

$$\mathbf{u}_{mod} = \begin{cases} \overline{\mathbf{u}_{ref}}^c & \text{when } |x_j - x_{cj}| \leq l_{cell}/2, \\ \mathbf{u}_{ref} & \text{otherwise,} \end{cases} \quad (2.2)$$

where  $\mathbf{u}_{ref}$  is the unperturbed flow, and an extra pressure step is applied after (2.2) to restore continuity at the edges of the cell. The experiment is repeated as many times as possible, applying it to different reference flow fields while changing the location and size of the perturbation cell.

Table 2 summarises the parameters of the experimental cells. They are expressed in terms of the distance from the wall to the bottom of the cell,  $y_{cell} = y_c - l_{cell}/2$ , which was found to collapse some results better than the cell centre, and are separated into two sets. In the first set, involving the 40 reference snapshots, perturbations are applied to a  $6 \times 6$  grid of cells evenly spaced in  $x$  and  $z$ , such that their centres are separated by  $\pi h/6$  in each



$l_{cell}^+$	$y_{cell}^+$ (set 1)	$y_{cell}^+$ (set 2)	Symbol
25	0, 12.5, 37.6, 62.6, 87.6, 113, 138, 163, 188, 213, 238, 288	0, 138	—
50	0, 25.0, 50.0, 75.0, 100, 125, 150, 175, 200, 225, 275	NA	▲
75	0, 12.6, 37.6, 62.6, 87.6, 113, 138, 163, 188, 213, 263	0, 38, 113, 188, 263	■
100	0, 25.0, 50.0, 75.0, 100, 125, 150, 175, 200, 250	NA	◆
150	0, 25.0, 50.0, 75.0, 100, 125, 150, 175, 225	0, 75, 225	●

Table 2. Parameters of the perturbation cells. See text for details.

direction (approximately 315 wall units). In the  $y$ -direction, perturbations are applied at the heights detailed in the second column of [table 2](#), ranging from cells touching the wall to those centred at the middle of the computational domain,  $y_c^+ \approx 300$ . Each of them is run for 0.65 turnovers, and consumes approximately 6 minutes in an Nvidia A100 GPU, so that the approximately 76 000 experiments in this set took 318 GPU-days.

While these experiments test a wide range of sizes at sparsely spaced locations across the flow, the ones in the last column of [table 2](#) aim to build heat maps that explore possible large-scale causality distributions not limited to a single cubical cell. Each reference snapshot is divided into a  $30 \times 30$  grid in the  $x$ - $z$  plane, approximately spaced by 75 wall units, and perturbations are centred at each point of that grid. For cells with  $l_{cell}^+ \geq 75$ , this procedure uniformly samples the whole plane, but due to its cost, it was limited to 20 initial snapshots and five different heights, each of which ran for only 0.49 turnovers. The resulting 180 000 tests took 565 GPU-days.

In both sets of experiments, the temporal evolution of the perturbation is measured by the energy of the perturbation velocity integrated over the whole computational domain,

$$\varepsilon_{\mathbf{u}}(t) = V^{-1} \int |\mathbf{u}_{mod} - \mathbf{u}_{ref}|^2 dV, \tag{2.3}$$

which evolves from some initial  $\varepsilon_{\mathbf{u}}(0)$  at the moment at which the perturbation is applied, to  $\varepsilon_{\mathbf{u}}(\infty) = 2K \equiv 2V^{-1} \int |\mathbf{u}|^2 dV$  when the reference and perturbed flow fields decorrelate after a sufficiently long time. For a chaotic system such as turbulence,  $\varepsilon_{\mathbf{u}}(\infty) \gg \varepsilon_{\mathbf{u}}(0)$ , and even if the evolution of the perturbation is far from linear over times of the order of a turnover, the perturbation energy typically grows almost exponentially for a while before levelling at  $\varepsilon_{\mathbf{u}}(\infty)$ . These considerations lead to two definitions of causal significance: an absolute one that disregards the initial perturbation magnitude and vanishes as  $t \rightarrow \infty$ ,

$$\sigma_{\mathbf{u}}(t) = \log_{10} \varepsilon_{\mathbf{u}}(t) / \varepsilon_{\mathbf{u}}(\infty) = \log_{10} \varepsilon_{\mathbf{u}}(t) / 2K, \tag{2.4}$$

and a relative one,

$$\sigma_{\mathbf{u}r}(t) = \log_{10} \varepsilon_{\mathbf{u}}(t) / \varepsilon_{\mathbf{u}}(0), \tag{2.5}$$

which measures relative growth and vanishes at  $t = 0$ . Both definitions typically grow with time, but we will be interested in cases in which the growth is particularly fast or slow, as defined by the top and bottom  $\phi$  percentile of the significance distribution. For most of the paper, experiments within the top  $\phi = 10\%$  of the significance distribution will be defined as ‘causally significant’, and those in the bottom 10%, as ‘causally irrelevant’. This fraction is broadly compatible with the percolation analysis often used to define thresholds. For example, the optimal percolation threshold in three-dimensional wall-bounded turbulence fills volume fractions of the order of 5%–10% (Jiménez 2018a),

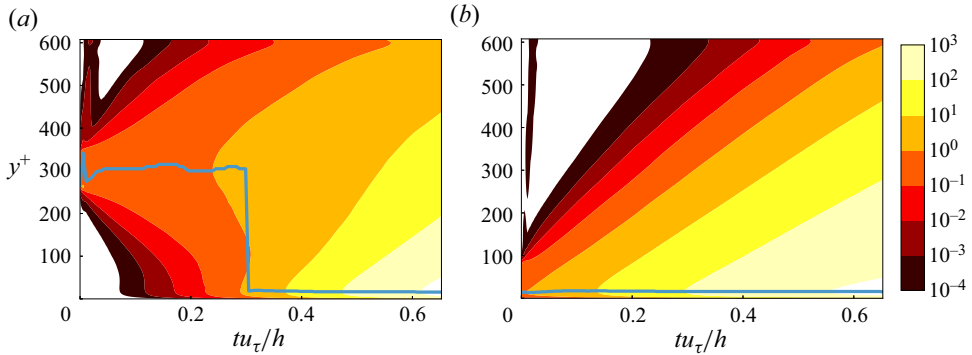


Figure 3. Plane-averaged perturbation magnitude  $\langle \varepsilon_u \rangle(y, t)$ , as defined in (3.1), unconditionally averaged over all perturbations with  $l_{cell}^+ = 75$  introduced at a given height, normalized with its maximum at  $t = 0$ . The blue line is the instantaneous position of the perturbation maximum. Contours are  $\langle \varepsilon_u \rangle(y, t) / \max_y \langle \varepsilon_u \rangle(y, 0)$ . Here, (a)  $y_c^+ = 300$ , (b)  $y_{cell} = 0$ .

while in two-dimensional vorticity fields, which are more directly comparable with the present application to individual planes, the covered area is closer to 20 %–30 % (Jiménez 2020a). Tests using  $\phi = 5\%$  or  $15\%$  showed few differences in the present results.

### 3. Temporal evolution of the significance

To further study the growth of the perturbations, we use its  $y$ -dependent averaged intensity,

$$\varepsilon_u(y, t) = (L_x L_z)^{-1} \iint |\mathbf{u}_{mod} - \mathbf{u}_{ref}|^2 dx dz, \quad (3.1)$$

equivalent to (2.3) but integrated over wall-parallel planes instead of over the whole domain, together with corresponding definitions for the significances. To minimise notational clutter, we use for them the same symbols as in (2.3)–(2.5), with the inclusion of  $y$  as a parameter. Figure 3(a) shows the growth of  $\varepsilon_u(y)$ , unconditionally averaged over all the perturbations introduced at a particular size and distance from the wall and normalised with its maximum at  $t = 0$ . The blue line is the position at which the perturbation is maximum. It initially stays at the height at which the perturbation is introduced, but a new peak grows near the wall and becomes dominant after  $tu_\tau/h \approx 0.3$ . In figure 3(b), where the perturbation is initially attached to the wall, the peak is always attached. During the very early stage of evolution ( $tu_\tau/h \lesssim 0.05$ ), a low-intensity perturbation spanning the whole channel appears in both cases. This is most likely due to the pressure pulse that enforces continuity at the edges of the perturbation cell, but it quickly dissipates and does not seem to influence later development.

Figure 4 shows the attachment time  $t_{att}$ , defined for individual tests as the moment when the perturbation maximum falls below  $y^+ = 50$ , and later averaged over the experimental ensemble. It is approximately proportional to  $y_{cell}$ , at least for  $y_{cell}^+ \gtrsim 50$ , with a propagation velocity  $dy_{cell}/dt = 1.37u_\tau$ . This is faster than the observed vertical advection velocity of coherent features in channels,  $dy/dt \approx \pm u_\tau$  (Lozano-Durán & Jiménez 2014b), and suggests that the perturbation is not simply advected by the flow, but actively amplified by it. In fact, the production term in the evolution equation for the perturbation energy is proportional to the mean shear (see Appendix A), and the most likely interpretation of figure 4 is that while all perturbations are advected to and from the wall by the background turbulence, those approaching the wall, where the shear is



Causal features in turbulent channel flow

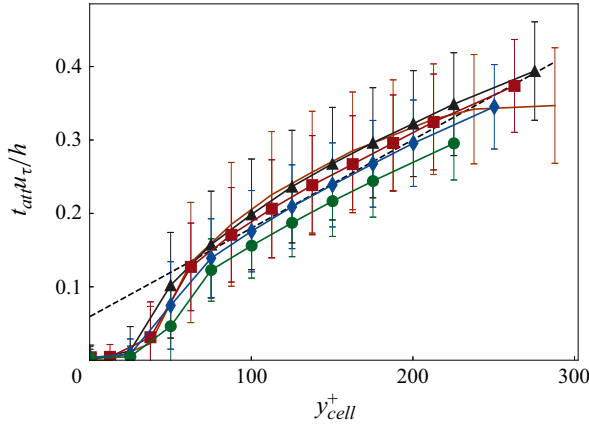


Figure 4. Attachment time  $t_{att}$  as a function of  $y_{cell}$ , for different  $l_{cell}$ . The dashed line is a least-squares fit to the curves with  $y_{cell} > 0$ , with slope  $dy/dt = 1.37u_\tau$ . Times are computed for individual tests, and symbols and bars are their averages and standard deviations. Symbols are as in table 2.

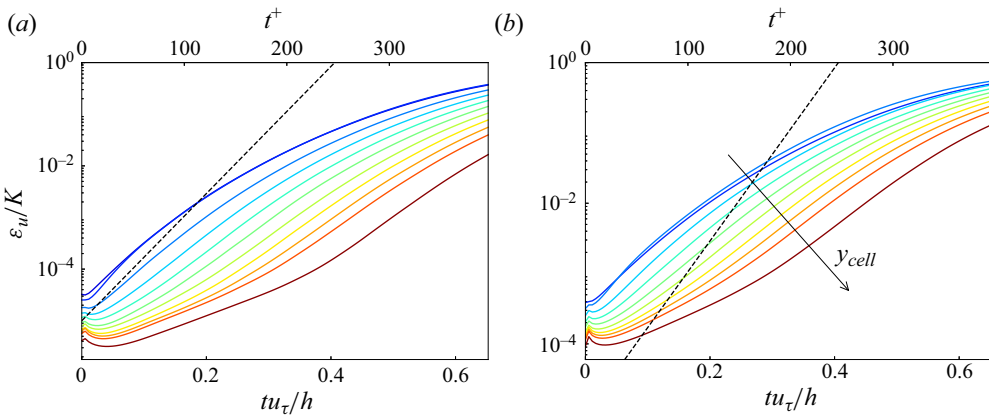


Figure 5. Temporal development of the unconditionally averaged domain-integrated perturbation  $\varepsilon_u(t)$ , as defined in (2.3), for (a)  $l_{cell}^+ = 50$ , (b)  $l_{cell}^+ = 100$ . In both plots, the cell distance from the wall increases from cold to warm colours, for the cases in table 2, and the diagonal dashed lines are the exponential Lyapunov growth rates from Nikitin (2018).

most intense, grow faster than those moving away from it, resulting in a mean downwards migration of the perturbation maximum. Notice, for example, the different slopes of downwards and upwards contours in figure 3. It is also relevant that  $t_{att}$  scales better with the distance from the wall to the bottom of the cell,  $y_{cell}$ , than with its centre,  $y_c$  (not shown), because it is the bottom that predominantly feels the stronger shear near the wall.

Figures 5(a,b) show two examples of the temporal evolution of the domain-integrated perturbation  $\varepsilon_u$ , using different cell sizes, and the line colour is the cell height. The figures show that  $\varepsilon_u$  is higher for larger cells, which is to be expected since it is an integrated quantity, and also for lower  $y_{cell}$ , also expected for a perturbation that removes velocity fluctuations, which are stronger near the wall. More interesting is that cells near the wall grow faster than those away from it, which may be understood as supporting the model in which their growth rate is controlled by the ambient shear.

The dashed straight lines in [figure 5](#) are the exponential growth rates from the Lyapunov analysis by Nikitin (2018), who reports a Lyapunov time for  $\varepsilon_u$  (the inverse of the leading exponent) of  $T_L^+ \approx 19$  ( $u_\tau T_L/h = 0.032$ ) in a turbulent channel at  $Re_\tau = 586$ . The leading Lyapunov vector is concentrated in the buffer layer, and the exponent scales in wall units, again consistent with a model in which the growth is controlled by the near-wall shear.

It is clear that our analysis shares many characteristics with the classical Lyapunov analysis, albeit with important differences. The most obvious is that the classical Lyapunov exponent assumes that the perturbation behaves linearly for an infinitely long time, while [figure 5](#) shows that our experiments saturate for times that, even if much longer than  $T_L$ , remain of interest for the flow evolution. A second important difference is that our initial perturbations, which are intended to probe the local structure of the flow rather than its mean properties, are compact with predetermined shapes, while those in Lyapunov analysis are allowed to spread across the flow field to their optimal structure. It may be relevant in this respect that there is an initial transient in which perturbations decay in most of our tests,  $u_\tau t/h \lesssim 0.1$ , and that this period is shorter for cells near the wall. This is reminiscent of the similar transient in Lyapunov calculations, during which perturbations align themselves to the most unstable direction. Our limited range of initial conditions is probably partly compensated by the substitution of the temporal averaging of classical analysis by averaging over tests, and it is interesting that the short-time growth rates of the smallest perturbations in [figure 5\(a\)](#), which mostly sample the buffer layer, approximately agree with Nikitin (2018). Larger or higher perturbations, which sample weaker shears, grow more slowly. We will provide in § 5.1 further support for the relevance of local shear to perturbation growth.

[Figure 6\(a\)](#) shows a typical evolution of the absolute significance  $\sigma_u$  for perturbations with a given  $l_{cell}$  and  $y_{cell}$ . Each of the grey lines is the result of a different experiment, and the red and blue lines are the mean evolutions of samples that are respectively classified as significant or irrelevant at  $t = 0$ . The bands are their standard deviations. The figure shows that the perturbations approximately maintain the ordering of their initial intensity. Initially stronger perturbations tend to remain strong for long times, although it follows from its definition that  $\sigma_u$  vanishes on average as  $t \rightarrow \infty$ . [Figure 6\(b\)](#) displays the persistence of the causality classification based of  $\sigma_u$ , defined as the fraction of samples identified as significant or irrelevant at  $t = 0$  that remain significant or irrelevant when classified at subsequent times. In the case illustrated in the figure, 34 % of the initially significant samples, and 29 % of the initially irrelevant ones, remain at the end of our experiments in the same class in which they were classified at  $t = 0$ . This fraction is at least 20 % in all the experiments in this paper, which is substantially higher than the 10 % expected from a random selection.

[Figure 6\(c\)](#) shows the evolution of the relative significance. Unlike the absolute significance,  $\sigma_{ur}$  vanishes at  $t = 0$  but does not reach the same long-time limit in all cases. In fact,  $\sigma_{ur}(\infty) = \log_{10}(2K) - \log_{10} \varepsilon_u(0)$ , and  $\sigma_{ur}(\infty)$  is essentially equivalent to the initial perturbation magnitude.

These considerations show that both  $\sigma_u$  and  $\sigma_{ur}$  characterise the evolution of the perturbations at short and intermediate times. The former mostly reveals that the perturbation intensity stays approximately proportional to its initial value for some time, while the latter, which compensates for this effect, describes its intrinsic growth. When  $\varepsilon_u \rightarrow 2K$  at longer times, the system forgets its initial conditions, and neither measure of significance is very useful.

Although [figure 6\(b\)](#) shows that the significance classification of a given experiment is not a completely random variable, the fact that the persistence is not unity implies that the

## Causal features in turbulent channel flow

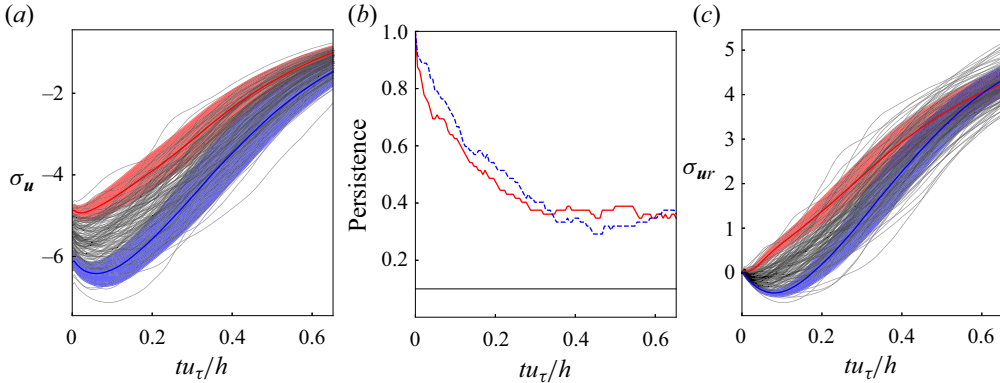


Figure 6. (a) Grey lines are the absolute significance  $\sigma_u$  (2.4) for individual experiments, as a function of time; only 20% of the total are included. The red and blue lines and their corresponding bands respectively represent the mean evolution and standard deviation of the samples diagnosed as significant or irrelevant at  $t = 0$ . (b) Fraction of experiments that continue to be classified as significant or irrelevant in terms of  $\sigma_u$  at different times, after being so classified at  $t = 0$ . Red indicates significant; blue indicates irrelevant. The black horizontal line is the probability threshold  $\phi = 10\%$ . (c) As in (a), for the relative significance  $\sigma_{ur}$  (2.5) diagnosed at  $tu_\tau/h = 0.29$ . In all cases,  $l_{cell}^+ = 50$ ,  $y_{cell}^+ = 125$ .

time at which the classification is performed is important. Consider, for example, the mean significance of the set  $\{I\}$  of tests classified at time  $t_c$  as irrelevant,  $\sigma_I(t_c) = N_{\{I\}}^{-1} \sum_{j \in \{I\}} \sigma_j$ , and define a similar  $\sigma_S(t_c)$  average for significant perturbations. The difference  $\sigma_S - \sigma_I$  typically increases initially and reaches a maximum before decaying at long times. The time  $t_{sig}$  at which this difference is maximum is also when the classification is less ambiguous, and we will preferentially use it from now on to define our significance classes.

Figures 7(a,b) show how  $t_{sig}$  changes as a function of  $l_{cell}$  and  $y_{cell}$ , using either  $\sigma_u$  or  $\sigma_{ur}$  as a causality measure. Disregarding the case  $l_{cell}^+ = 25$ , which is well within the dissipative range of scales and tends to behave differently from larger cells,  $t_{sig}$  is explained mainly by  $y_{cell}$ , and it is clear that  $\sigma_{ur}$  is a better indicator for this purpose than  $\sigma_u$ . We will mostly use it from now on. It is interesting that  $t_{sig}$  is very close to, and generally slightly larger than, the attachment time  $t_{att}$  in figure 4, as shown by the difference of the two values in figure 7(c), suggesting again that the arrival of the disturbances to the wall is an important factor in determining causality.

We have seen above that the initial intensity of the perturbations has an effect on their subsequent evolution. This is also true of our significance classification, and can be quantified by the correlation of  $\sigma_{ur}(t_c)$  with  $\varepsilon_u(0)$  (not shown). This correlation tends to  $-1$  at long times, as explained above, but remains moderately positive for  $t_c \lesssim t_{sig}$ , confirming that the initial relative growth rate for strong perturbations is faster than for weak ones. In most cases,  $t_{sig}$  approximately coincides with the moment at which the correlation changes sign and is close to zero, making the classification relatively independent of the initial perturbation intensity. At this moment, the energy of the perturbation is still a small fraction of the total energy of the flow. Taking as an example the topmost curve in figure 5(b) ( $l_{cell}^+ = 100$ ,  $y_{cell} = 0$ ), the average energy of the initial perturbations is approximately  $3 \times 10^{-4} K$ , and grows to  $0.6K$  at the end of the experimental runs, but it is still  $8 \times 10^{-3} K$  at the optimal classification time  $t_{sig} \approx 0.17h/u_\tau$ . This does not mean that the perturbation can be linearised up to that

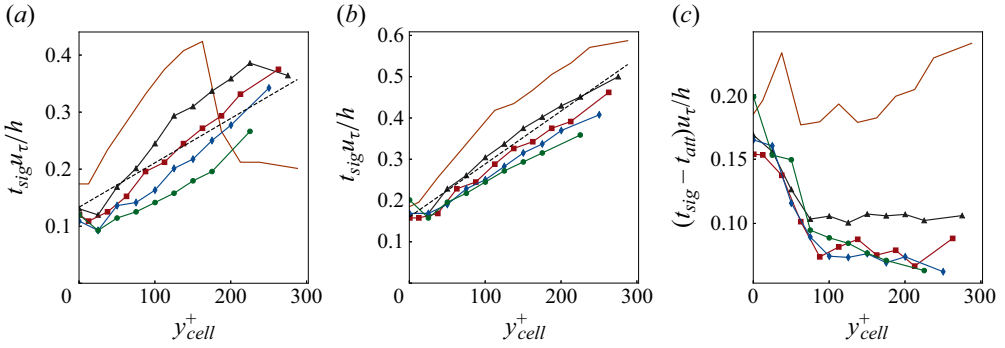


Figure 7. Optimal classification time  $t_{sig}$  as a function of  $y_{cell}$ . Symbols as in table 2. The dashed lines in (a,b) are least-squares linear fits, whose slope is  $dy/dt = 2.12u_\tau$  in (a) and  $dy/dt = 1.28u_\tau$  in (b). (a) Using  $\sigma_u$ ; (b) using  $\sigma_{ur}$ . (c) Offset between the  $\sigma_{ur}$  classification time and the attachment time.

time. The intensity of the perturbation is always  $O(K)$ , and the growth of its integrated energy is mostly due to its geometric spreading (see figure 2).

#### 4. Diagnostic properties for causal significance

Having described how the significance of an initial condition can be characterised, we recover our original task of determining which properties of the perturbed cells are responsible for their causality. The basic assumption is that the characterisation of causality can be reduced to a single observable of the cell at the perturbation time,  $t = 0$ , such as its average vorticity, rather than requiring several conditions to be satisfied simultaneously, or even some property of the extended environment of the cell, or of its history. As mentioned in the Introduction, the strategy is to perform many experiments modifying individual cells, to label them according to their significance at some later time, and to test which cell observables at  $t = 0$  can be used to separate the classes thus labelled. Hereafter, the one-point scalar  $\langle f \rangle_c$  stands for the cell average of a property:

$$\langle f \rangle_c = l_{cell}^{-3} \int_{y_{cell}}^{y_{cell}+l_{cell}} \int_{x_c-l_{cell}/2}^{x_c+l_{cell}/2} \int_{z_c-l_{cell}/2}^{z_c+l_{cell}/2} f(x, y, z) dx dy dz. \quad (4.1)$$

Following Jiménez (2020b) and Encinar & Jiménez (2023), the ranking of observables uses a linear-kernel support vector machine (SVM) (Cristianini & Shawe-Taylor 2000), implemented in the scikit-learn Python library (Pedregosa *et al.* 2011), which determines an optimal separating hyperplane between two pre-labelled data classes. In our case, we look for the optimal separation of significant or irrelevant experiments in terms of a single quantity, and the SVM hyperplane reduces to a threshold. For each combination of  $l_{cell}$  and the  $y_{cell}$  values in the second column of table 2, and for each classification time  $t_c$ , two-thirds of the initial conditions are collected into a training set, with the remaining third reserved for testing. The 10% most significant experiments of the training set are labelled as significant, and the bottom 10%, as irrelevant. The remaining 80% are not used for classification purposes. An optimum partition threshold is computed for each of the observables detailed below, and an SVM classification score is assigned to each observable using the test set. The score measures the fraction of data allocated to their correct class by the SVM threshold, and ranges from unity for perfect separability to 0.5 for cases in which the two classes are fully mixed. The procedure is repeated three times

$\langle u_i \rangle_c, \langle \omega_i \rangle_c$	Mean velocities and vorticities
$\langle u_i^2 \rangle_c$	Kinetic energy
$\langle uv \rangle_c, \langle (uv)^2 \rangle_c$	Mean and mean-squared Reynolds product
$\langle u_i^2 \rangle_c, \langle \omega_i^2 \rangle_c$ (no sum over $i$ )	Mean-squared components
$\langle Prod \rangle_c = -\langle uv \partial_y U \rangle_c$	Mean energy production
$\langle Tdif \rangle_c = -\langle \partial_y v u_i^2 \rangle_c / 2$	Mean energy transport
$\langle \partial_y u \rangle_c$	Mean shear
$\langle \partial_y u \rangle_{\beta w}$	Mean shear using only $y^+ > 5$
$\langle \partial_i u_i \rangle_c$ (no summation)	Mass conservation

Table 3. Cell observables. All averages are taken over cells at  $t = 0$ .

$\varepsilon_u, \varepsilon_\omega$	Mean-squared velocity and vorticity fluctuations
$\langle \omega_i^2 \rangle_c, \langle s_{ij} s_{ij} \rangle_c$	Enstrophy, strain
$u_i'^c, \omega_i'^c$ (no sum over $i$ )	In-cell standard deviations
$\langle P_{\varepsilon u} \rangle_c, \langle C_{\varepsilon u} \rangle_c, \langle D_{\varepsilon u} \rangle_c$	Production, transport and dissipation of $\varepsilon_u$ (Appendix A)

Table 4. As in table 3, for observables describing perturbation and small-scale quantities.

after randomly separating the data into training and test sets, and the diagnostic score for the observable is defined as the average of the three results.

The whole process can be automated and is reasonably fast. The experimental description in § 2.1 shows that each SVM run is only requested to classify two sets of 96 points each, and to test the classification on two sets of 48 points. This allows us to minimise pre-existing biases by testing many possible observables. The robustness of the classification results was assessed by decreasing the number of samples by half.

The observables can be physically classified into average cell properties, such as kinetic energy, and perturbation or small-scale properties, such as the kinetic energy of the velocity fluctuations with respect to the cell mean. The former are summarised in table 3, and the latter in table 4. In both cases, properties that are statistically symmetric with respect to reflections on  $z$  are used as absolute values, and positive definite quantities, such as mean squares, are used as logarithms. Otherwise, all observables are processed in the same way.

The diagnostic score of an initial condition depends on the cell height, on its size, and on the moment at which it is classified. Figure 8 shows a typical table of the three best observables identified by the absolute significance  $\sigma_u$ , as functions of the classification time. Cells are coloured by the classification score. In all cases, the best observable is the initial perturbation amplitude  $\varepsilon_u$ , a related quantity such as  $\varepsilon_\omega$ , or the viscous dissipation of the perturbation intensity  $\langle D_{\varepsilon u} \rangle_c$ . Although not included in the table, the next best observable is usually also a small-scale quantity closely correlated with the intra-cell velocity fluctuations, such as  $s_{ij} s_{ij}$ ,  $\omega_i^2$  or the in-cell standard deviation  $v'^c$ . The table in figure 8 is thus equivalent to the fluctuation persistence in figures 6(a,b).

In the sense that this absolute persistence is due to the slow relaxation of the initial amplitude, it can be considered physically uninteresting, but it can be largely compensated by using the relative significance  $\sigma_{ur}$  defined in (2.5). Figure 9 displays the two best observables for different sizes at a fixed cell height, and figure 10 displays results for a given size and different heights. In both cases, the best score starts being relatively high at short classification times, decreases for intermediate ones, and increases again towards

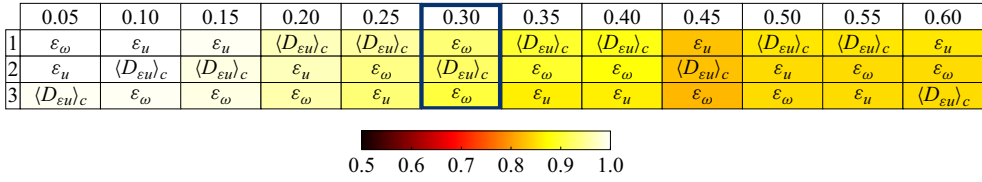


Figure 8. Classification score of the three best observables for a classification based on absolute significance  $\sigma_u$ . Row indicates rank; column indicates evaluation time in turnovers. The highlighted column is  $t_{sig}$ . Colour indicates the classification score. Here,  $l_{cell}^+ = 50, y_{cell}^+ = 125$ .

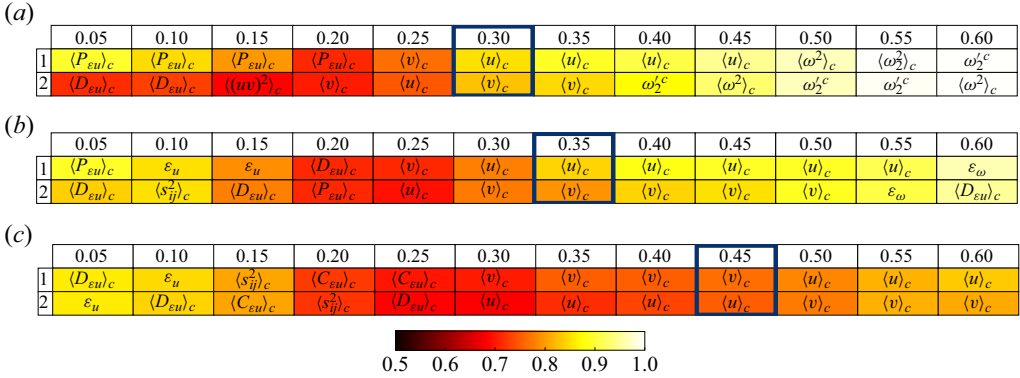


Figure 9. Classification score of the two best observables for a classification based on relative significance  $\sigma_{ur}$ : (a)  $l_{cell}^+ = 150, y_{cell}^+ = 150$ , (b)  $l_{cell}^+ = 75, y_{cell}^+ = 138$ , (c)  $l_{cell}^+ = 25, y_{cell}^+ = 138$ . Row indicates rank; column indicates evaluation time in turnovers. The highlighted columns are  $t_{sig}$ . Colour indicates classification score. Here,  $y_{cell}^+ \approx 150$ .

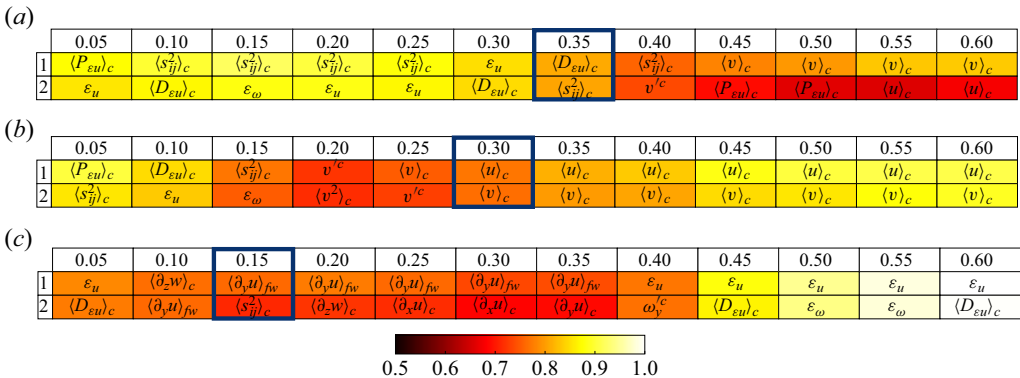


Figure 10. Classification score of the two best observables for a classification based on relative significance  $\sigma_{ur}$ : (a)  $y_{cell}^+ = 275$ , (b)  $y_{cell}^+ = 125$ , (c)  $y_{cell} = 0$ . Row indicates rank; column indicates evaluation time in  $h/u\tau$ . The highlighted columns are  $t_{sig}$ . Colour indicates classification score. Here,  $l_{cell}^+ = 50$ .

the end of the experimental run. The evolution of the optimum diagnostic variables with the classification time can be divided into three phases.

During the initial phase, up to the time when the scores are lowest, the best observables include  $s_{ij}s_{ij}$ , the magnitude of the initial disturbance, and the disturbance production and dissipation, all of which are either highly correlated with the initial value of  $\varepsilon_u$ , or are



terms in its evolution equation (A8). This part of the table is equivalent to the observation in § 2.1 that initially stronger perturbations not only remain strong, but also grow faster than weaker ones.

The second phase is the broad minimum of the score around  $t_{sig}$ . While the scores in this phase are not high, the best observables change from the small-scale perturbation properties of the initial phase to properties of the cell that do not include fluctuations, such as the cell average of some velocity component, or equivalently, the mean shear when the cells are very close to the wall. It is interesting that the best measure of shear near the wall is  $\langle \partial_y u \rangle_{fv}$ , which excludes the viscous sublayer (see figure 10c). This is consistent with the idea that the growth of the perturbation is due to the energy production by the local shear, because the fluctuation production term in Appendix A is proportional to the shear, but also to the Reynolds stresses  $\hat{u}_i \hat{u}_j$ , which are inactive in the sublayer.

It is interesting that the longitudinal velocity derivatives  $\langle \partial_x u \rangle_c$  and  $\langle \partial_z w \rangle_c$  appear among the most diagnostic cell properties for wall-attached perturbations in figure 10(c). These derivatives are involved in mass conservation, and follow naturally from the meandering of near-wall streaks, which has been associated with streak breakdown (Jiménez & Moin 1991; Hamilton *et al.* 1995; Waleffe 1997) and with the generation of Orr bursts (Orr 1907; Jiménez 2013). Although not apparent from figure 10(c), it can be shown that significant cells are associated with  $\partial_x u < 0$ ,  $\partial_z w > 0$ , with the opposite association for irrelevant ones.

Finally, at longer times of the order of  $t - t_{sig} \approx 0.25h/u_\tau$ , the score recovers, and the most diagnostic observable reverts to the small-scale quantities that dominate short times. Since we saw in § 2.1 that  $\sigma_{ur}$  at long times is essentially equivalent to  $\varepsilon_u(0)$ , this final phase is a reflection of the behaviour at short times, and does not represent new physics.

Figure 11(a) shows the dependence on  $y_{cell}$  of the time at which the accumulated score of the top four observables reaches its minimum. After an initial transient that gets shorter as the cell size increases,  $t_{min}$  grows with the distance from the wall, and approximately tracks the optimum classification time  $t_{sig}$ .

Figures 11(b–f) summarise the evolution of the scores as functions of time. The blue lines are averages of the scores of several fluctuation quantities, and the red lines are averages of cell-scale properties. The figures are offset by their attachment time  $t_{att}$ , which improves their collapse significantly, and reflect the decreasing influence of the small-scale quantities as the perturbations approach the attachment time, as well as the increasing importance of the cell-scale properties as the perturbations intensify. It should be mentioned that offsetting  $t$  with the optimum classification time  $t_{sig}$ , instead of with  $t_{att}$ , also collapses most scores, as could be expected from the similarity of both times in figure 7. It also collapses better the case  $y_{cell} = 0$ , which is not included in figure 11, and for which  $t_{att}$ , defined at the arbitrary distance  $y^+ = 50$ , does a poor job. In spite of this,  $t_{att}$  is used in figure 11 because it improves the case  $l_{cell}^+ = 25$ , and underscores the already mentioned connection between significance and the energy production from the near-wall shear. It is also interesting that the score of the velocities has a secondary maximum at  $t = 0$ , probably due to the known correlation of small-scale vorticity with the large-scale streamwise-velocity streaks (Tanahashi *et al.* 2004).

From now on, we will mostly focus on results of the relative significance classified at  $t_{sig}$ , for which the optimum observables are collected in figure 12. As seen above, they are mostly the average cell velocities,  $\langle u \rangle_c$  or  $\langle v \rangle_c$ . The exceptions are cells in the buffer layer  $y_{cell}^+ \lesssim 50$ , in which shear can probably be taken as a proxy for the streamwise velocity, and cells with  $l_{cell}^+ = 25$  very far from the wall. We have already mentioned that these perturbations are probably too small to survive for the relatively long times required

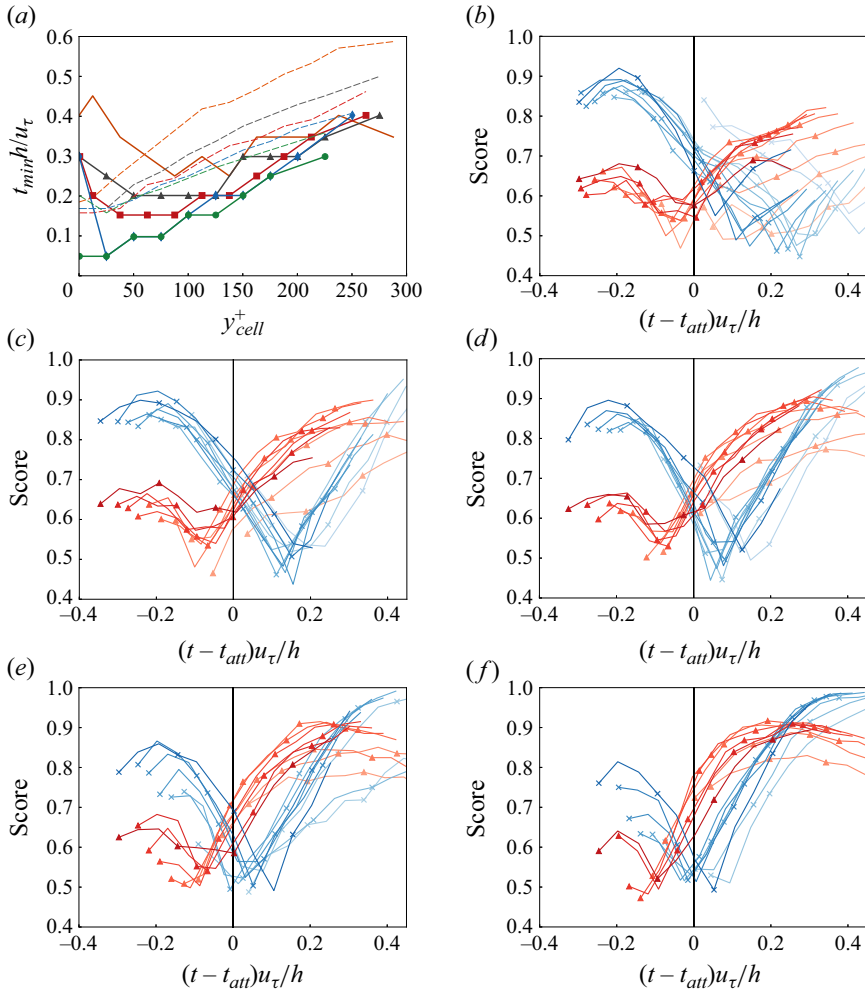


Figure 11. (a) The solid lines are the time  $t_{min}$  at which the sum of the scores of the four best observables is lowest. The dashed lines are  $t_{sig}$  from figure 7(b). Other symbols are as in table 2. (b–f) Classification scores of selected observables as functions of time, computed from  $\sigma_{ur}$ . Crosses indicate small-scale quantities, defined as the average of the scores of  $\varepsilon_u$  and  $\langle s_{ij}s_{ij} \rangle_c$ . Triangles indicate cell-scale quantities, average of  $\langle u \rangle_c$  and  $\langle v \rangle_c$ . Abscissae are offset by the attachment time  $t_{att}$ . Colour intensity increases with the distance from the wall, from  $y_{cell}^+ = 12.5$  to  $y_{cell}^+ = 275$ , with (b)  $l_{cell}^+ = 25$ , (c)  $l_{cell}^+ = 50$ , (d)  $l_{cell}^+ = 75$ , (e)  $l_{cell}^+ = 100$ , (f)  $l_{cell}^+ = 150$ .

to reach the wall, in agreement with the assimilation results from Wang & Zaki (2022) mentioned in the Introduction.

### 5. Conditional flow fields

While we have seen that the cell-averaged velocity fluctuations are diagnostic quantities for causality, our analysis did not include their sign. Figures 13–15, which display averaged velocity fields conditioned to the position of significant or irrelevant perturbation cells, shows that the sign is important.

Figure 13 displays longitudinal ( $x$ – $y$ ) sections of the streamwise and wall-normal velocities, conditioned to either significant (figures 13a,c,e) or irrelevant (figures 13b,d,f)

## Causal features in turbulent channel flow

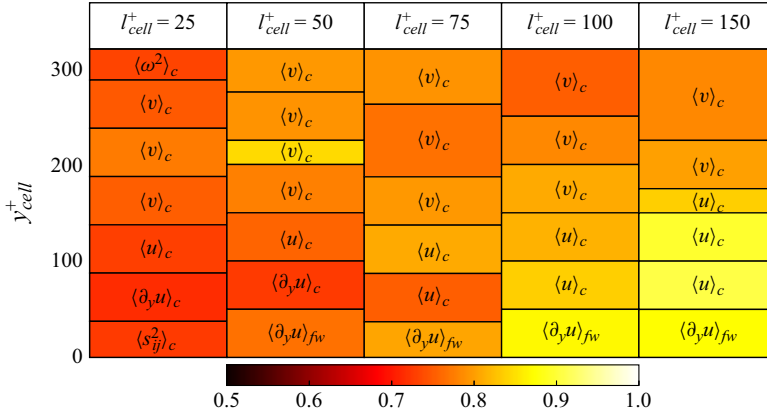


Figure 12. Best observable at  $t_{sig}$ . Colour indicates score. The bottom of each tile in the figure aligns with the left-hand  $y_{cell}$  axis.

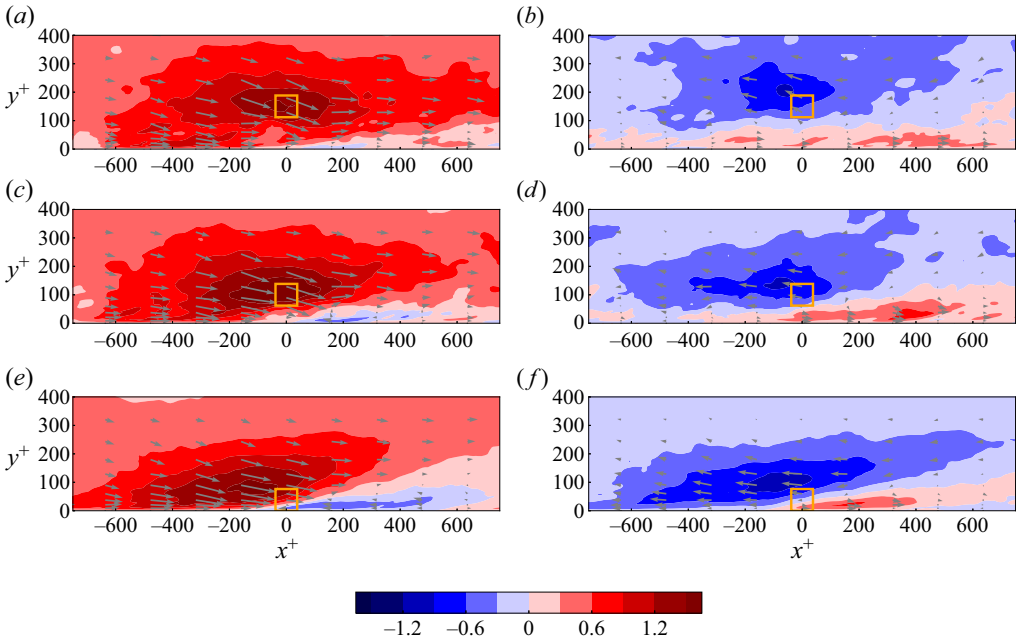


Figure 13. Streamwise section at  $z = z_c$  of the conditional velocity field of the reference flow at  $t = 0$  around the perturbation cell. The colour background is the conditional streamwise velocity. Arrows are velocity fluctuation vectors parallel to the plane of the figure, and the light-coloured box is the perturbation cell. Here,  $l_{cell}^+ = 75$ , and (a,b)  $y_{cell}^+ = 113$ , (c,d)  $y_{cell}^+ = 62.6$ , (e,f)  $y_{cell} = 0$ . (a,c,e) Significant, (b,d,f) irrelevant.

cells. It is evident that the former are biased towards fourth-quadrant regions ( $u > 0$ ,  $v < 0$ ), while the latter are in second-quadrant regions ( $u < 0$ ,  $v > 0$ ) (Lu & Willmarth 1973).

The three rows in figure 13 corresponds to perturbations introduced at decreasing distances from the wall. The frames are centred at the streamwise position of the perturbation cell, and the figure shows a fluid wedge entering the frame from its downstream right-hand edge, becoming more prominent as the cell approaches the wall.

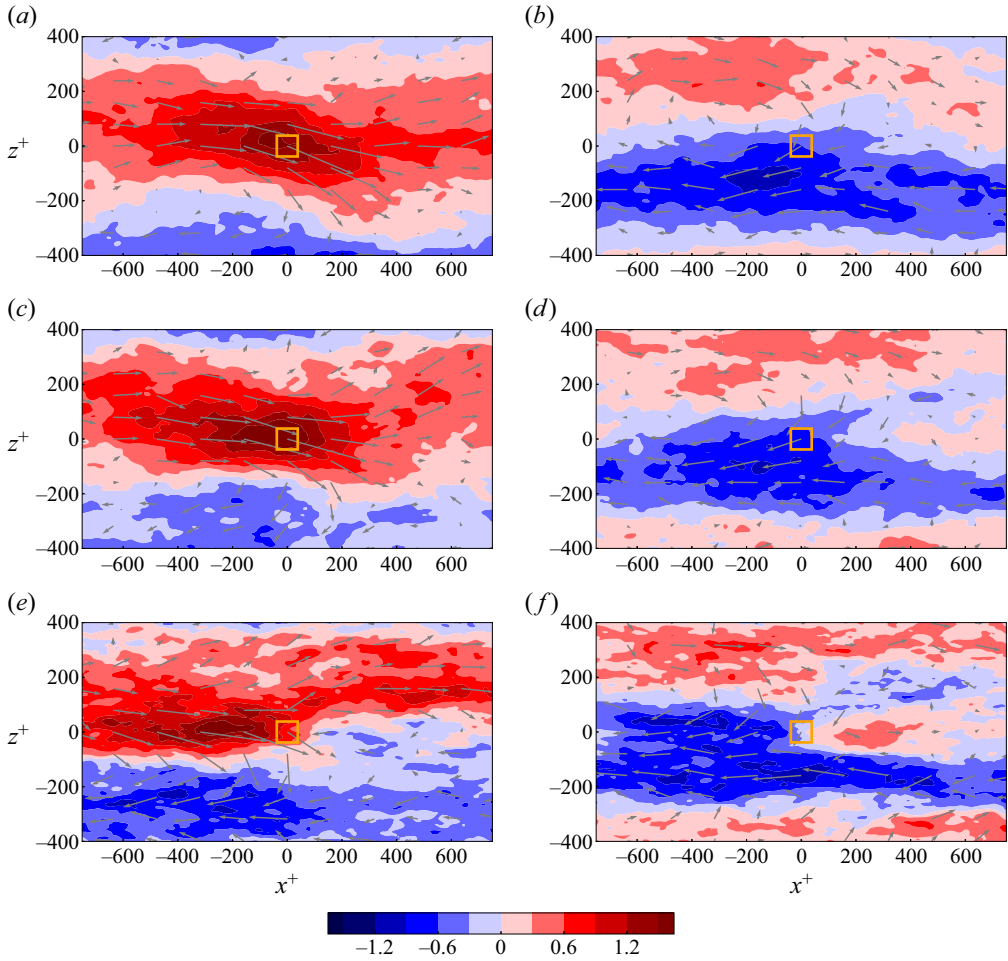


Figure 14. As in figure 13, for a wall-parallel section at  $y = y_c$ .

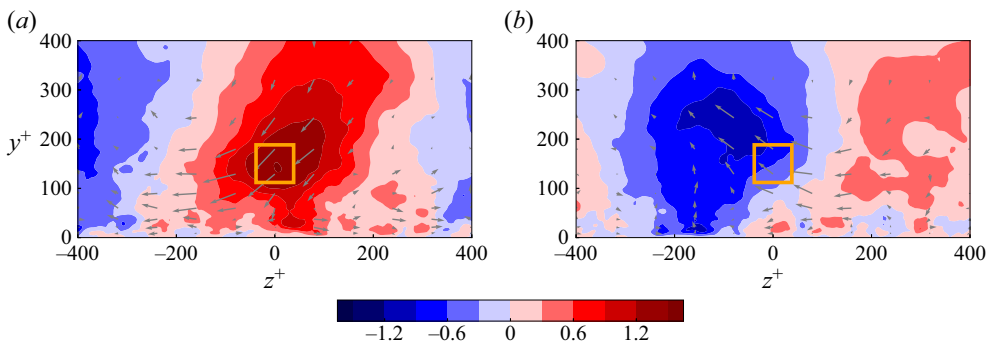


Figure 15. As in figures 13(a,b), for the  $(z-y)$  cross-flow section at  $x = x_c$ . (a) Significant, (b) irrelevant, for  $y_{cell}^+ = 113$ ,  $l_{cell}^+ = 75$ .

At the same time, there is an upstream drift of the darker core of the velocity distribution. This is clearest in the significant cases in figures 13(a,c,e), where the incoming wedge is low-speed fluid, but it can also be traced in the irrelevant cases in figures 13(b,d,f). The result is that the position of the causally significant cells moves downstream towards an interface at which high-speed fluid overtakes a low-speed one. Irrelevants are associated to an interface in which low-speed fluid is left behind by higher speed ahead of it.

Figure 14 displays wall-parallel ( $x$ - $z$ ) sections of the same cases as figure 13, and figure 15 shows cross-flow ( $z$ - $y$ ) sections of figures 13(a,b). There is no orientation ambiguity in the longitudinal sections in figure 13, but figures 14 and 15 would be statistically symmetric even if individual flow fields were not. To preserve possible systematic asymmetries, the  $z$  coordinate of all the flow fields is reflected so that the spanwise velocity averaged over a cube of side  $3l_{cell}$ , centred at the perturbation cell and possibly truncated by the wall, is  $\langle w \rangle_{3c} < 0$ . The orientation of the sections in figures 14 and 15 is therefore not physically meaningful, but the asymmetry of the different frames is consistent and complements the information in figure 13.

Figure 14 shows that the velocity interfaces in figure 13 correspond to kinks in the large-scale streaks that dominate the flow.

Although the frames in figures 13 and 14 represent unrelated experiments, it is tempting to interpret them as a temporal evolution in which perturbations introduced farther from the wall correspond to earlier times, and travel downstream and towards the wall until they reach it at  $t_{att}$  (or  $t_{sig}$ ). The velocity maximum in figures 14(a,c,e) shifts by  $\Delta x^+ \approx 200$  from the top to the bottom row of frames. Assuming, from figure 4, that  $u_\tau t_{att}/h \approx 0.2$ , this corresponds to a velocity difference  $\Delta u^+ \approx 1.5$ , which is a reasonable estimate for the difference in the advection velocity of features in a high-velocity streak with respect to the average flow velocity (Krogstad, Kaspersen & Rimestad 1998; Lozano-Durán & Jiménez 2014b).

Interestingly, the streamwise drift of the irrelevant velocity features in the right-hand columns of figures 13 and 14 is less clear than in the significant ones in the left-hand columns. The environment of the irrelevants can rather be described as an interface that gets wider as the cell approaches the wall. The flow cross-sections in figure 15 support this description, and the combined evidence from the three sets of sections is consistent with a model in which causally significant cells are associated with the front of a high-speed sweep that steepens as it approaches the wall and overtakes a lower-speed region. Conversely, irrelevant cells are located at the trailing end of a high-speed region that leaves behind a lower-speed flow. We may recall at this point that the table in figure 10(c) showed that the wall-parallel mass conservation derivatives are diagnostic of causality near the wall, and that while  $\partial_x u < 0$  signals significance,  $\partial_x u > 0$  signals irrelevance. This asymmetry suggests that the generation of structures strong enough to have a global effect on the flow depends on mass conservation failures when streaks of different velocity run into each other. This is most probably due to meandering, as in figures 14(a,c,e), and the effect is strongest when this happens within the strong shear near the wall. The trailing edges of the meander, as in figures 14(b,d,f), or the tails at which high-speed streaks pull away from low-speed ones, are passive.

The association of strong near-wall  $v$  structures with the downstream end of high-speed streaks and with the upstream end of low-speed ones was already noted by Jiménez, del Álamo & Flores (2004) and Jiménez & Kawahara (2013). Their interpretation was that  $v$  creates the streaks, but the arguments above, together with the fact that causality can be traced to flow locations far from the wall, suggest that the sequence of events is the other way around, and that the formation of near-wall bursts depends on continuity failures of non-uniform  $u$  streaks.

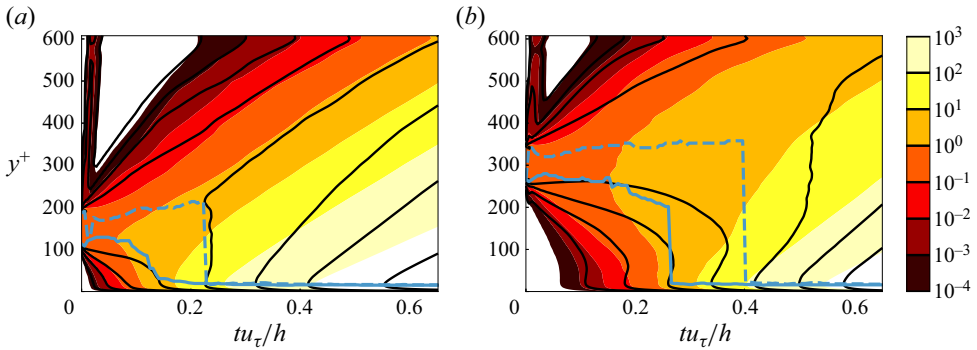


Figure 16. Plane-averaged perturbation magnitude  $\langle \varepsilon_u \rangle(y, t)$ , as defined in (3.1), conditionally averaged over significant or irrelevant perturbations and normalised with the maximum of the conditioned initial value. The bold cyan lines are the instantaneous position of the perturbation maximum. Filled contours and the solid cyan line are significant; line contours and the dashed cyan line are irrelevant. Contour levels are  $\langle \varepsilon_u \rangle(y, t) / \max_y \langle \varepsilon_u \rangle(y, 0)$ . Classification is done at  $t_{sig}$  using  $\sigma_{ur}$ , and  $l_{cell}^+ = 75$ , with (a)  $y_{cell}^+ = 113$ , (b)  $y_{cell}^+ = 263$ .

### 5.1. The shear time

Figure 16 is similar to the evolution of the plane-averaged fluctuation magnitude in figure 3, but is here separated into conditionally significant cases (filled contours) and irrelevant ones (lines). In both cases, as well as in the unconditional evolution in figure 3, the perturbation initially remains at the height at which it is introduced, before spreading vertically. All perturbations eventually fill the channel, as expected for a chaotic system, but the growth is faster in the significant cases. The bold cyan lines in figure 16 are the wall-normal position of the perturbation maximum. It is clear that the solid lines representing significant perturbations initially trend downwards and attach to the wall faster than the dashed lines representing irrelevant perturbations, which initially trend away from the wall or drift little. This supports the interpretation that significant perturbations are sweep-like, and the conjecture in §§ 3 and 4 that causal significance depends on the amplification of perturbations by the strong shear near the wall.

This is tested directly in figure 17. Figure 2 shows that perturbations spread with time along the three directions, and that it is difficult to define an instantaneous location to measure the shear that they encounter, but figures 3 and 16 suggest that it is possible to define an effective shear by weighting the mean velocity profile, which depends only on  $y$ , with the perturbation magnitude

$$S_\varepsilon(t) = \frac{\int \varepsilon_u(y, t) \partial_y U(y) dy}{\int \varepsilon_u(y, t) dy}, \quad (5.1)$$

and a dimensionless effective shear time

$$T_S(t) = \int S_\varepsilon dt. \quad (5.2)$$

Figure 17(a) illustrates the development of the relative growth of causally significant and irrelevant perturbations in terms of the global eddy turnover time. The significant perturbations grow from the start, while the irrelevant ones initially decay and only later grow to match the causal case. Most of the initial decay and of the slow growth of



## Causal features in turbulent channel flow

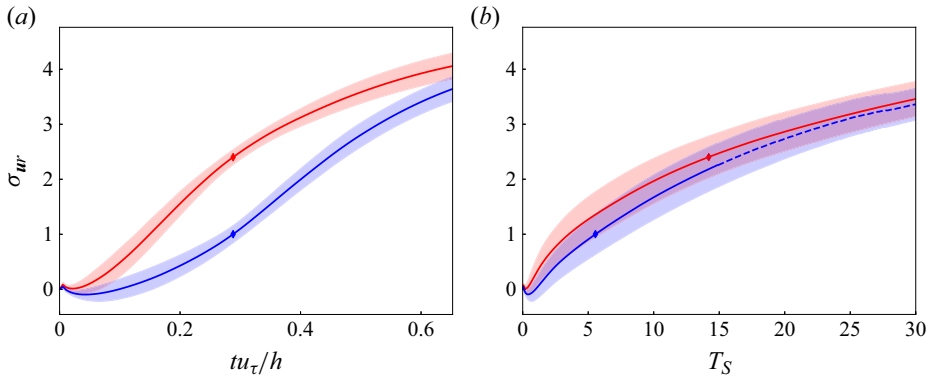


Figure 17. Relative perturbation growth  $\sigma_{ur}(t)$  conditioned to significant (red) and irrelevant (blue) samples, classified at  $t_{sig}$ . Solid line indicates the mean; shading indicates the standard deviation;  $\blacklozenge$  indicates  $t_{sig}$ . (a) In eddy turnovers; (b) normalised by the local shear time, as in (5.2). The dashed part of the irrelevant line in (b) corresponds to times for which not all experiments are available, because some of them end within the plot. Here,  $l_{cell}^+ = 75$ ,  $y_{cell}^+ = 133$ .

irrelevants can be attributed to their failure to initially approach the wall. Figure 17(b) plots the same data using the local shear time computed for individual experiments. The two evolutions now approximately coincide, supporting the importance of the local shear, and providing an explanation for the association of sweep-like flows with causality. The effect of the negative wall-normal velocity is to bring perturbations close to the wall. Ejection-like regions move perturbations away from the wall to layers where the shear is low, and they become causally relevant only after they eventually diffuse into the near-wall layer.

The collapse with the shear time applies only to significant and irrelevant perturbations at the same distance from the wall. Perturbations introduced at different distances behave differently, at least at the relatively low Reynolds number of our experiments for which self-similar behaviours with respect to  $y$  are necessarily limited.

### 5.2. Geometry of causal events

While we have seen that significant and irrelevant cells are associated with sweep- and ejection-like regions of the flow, it remains unclear whether the quadrants discussed in the previous section are the same as the intense events traditionally associated with sweeps and ejections in wall turbulence (Lu & Willmarth 1973). This is the purpose of the experiments in the second column of table 2, which cover selected wall-parallel planes with a dense grid of perturbation experiments.

Figure 18 displays the resulting quadrant plot, drawn for cell-average quantities. The line contours are the unconditional joint probability density function of  $\langle u \rangle_c$  and  $\langle v \rangle_c$ , while the coloured ones are conditioned to either significant cells in figure 18(a), or irrelevants in figure 18(b). The hyperbolic lines in the figure are intensity limits for sweeps and ejections, defined as

$$|\langle u \rangle_c(\mathbf{x}) \langle v \rangle_c(\mathbf{x})| \geq H_{\pm} \langle u \rangle'_c(y) \langle v \rangle'_c(y). \quad (5.3)$$

In the classical quadrant plot for point velocities, the threshold  $H$  depends only on  $y$  (Lozano-Durán *et al.* 2012), and results in different volume fractions for sweeps and for ejections (see the last row of table 5). To facilitate comparison with our choice of a common area fraction for significant and irrelevant cells, figure 18 uses two different

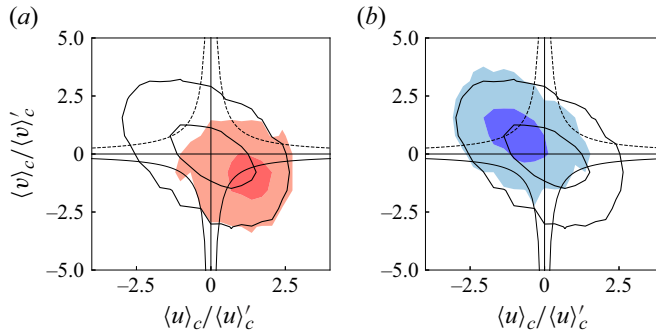


Figure 18. Joint probability density function of the cell-averaged velocities. Line contours are unconditional. Filled ones are conditioned to (a) significant cells, (b) irrelevant. Both contain 60% and 99% of the data, and  $y_{cell}^+ = 113$ ,  $l_{cell}^+ = 75$ . The solid hyperbolae are the  $H_-$  threshold that isolates the 10% most intense velocity quadrants with  $\langle v \rangle_c < 0$ , as in (5.3), and the dashed hyperbolae are  $H_+$  for  $\langle v \rangle_c > 0$ .

$y_{cell}^+$	$H_-$	$H_+$	$S_1$ (%)	$S_2$ (%)	$S_3$ (%)	$S_4$ (%)
1	0.74	0.75	4.17	45.94	3.14	46.75
38	0.77	0.87	2.58	47.17	1.81	48.44
113	0.80	1.03	1.44	48.08	2.00	48.47
188	0.76	1.04	1.39	48.17	2.72	47.72
263	0.75	0.99	0.92	48.25	4.14	46.69
—	1.75	1.75	4.40	61.54	6.59	27.47

Table 5. Parameters of intense quadrant structures for cell-averaged velocities, compiled over wall-parallel planes for  $l_{cell}^+ = 75$ . The thresholds  $H_-$  and  $H_+$  are as in figure 18, and the  $S_j$  are the fraction of the intense area associated with each quadrant. The bottom row gives volume fractions for pointwise quadrant structures in the  $Re_\tau = 935$  channel of Lozano-Durán, Flores & Jiménez (2012), in which the combined intense quadrants fill 9% of the channel volume.

thresholds:  $H_-$  for sweep-like structures with  $\langle v \rangle_c < 0$ , and  $H_+$  for ejection-like ones with  $\langle v \rangle_c > 0$ . They are adjusted so that the total areas for sweeps and for ejections are the ones used for the significance analysis,  $\phi = 10\%$ . They are given in table 2 for the five experimental wall distances, and are lower than the  $H \approx 1.75$  used in Lozano-Durán *et al.* (2012) and in other studies. Correspondingly, they select a larger area fraction, 20% in total, rather than the approximately 9% volume fraction in Lozano-Durán *et al.* (2012). However, table 5 shows that the distribution of quadrants in these intense regions is not very different from the classical values, once the relative fractions of sweep- and ejection-like structures are taken into account. As in the case of point velocities, most strong structures are either pure sweeps,  $\langle u \rangle_c > 0$ ,  $\langle v \rangle_c < 0$ , or pure ejections,  $\langle u \rangle_c < 0$ ,  $\langle v \rangle_c > 0$ , and there are comparatively few intense  $Q_1$  or  $Q_3$ . The filled contours in figure 18(a) are cell-averaged velocities of the significant cells, and those in figure 18(b) are irrelevant ones. It is evident that significant structures tend to be in strong  $Q_2$  sweeps, while irrelevant structures are in strong  $Q_4$  ejections.

This association is quantified in figure 19. The area fraction of the intersection between two classes,  $A$  and  $B$ , is defined as  $\Gamma(A, B) = 2S(A \cap B)/(S(A) + S(B))$ , where  $S$  denotes the area covered by each class. Figure 19(a) shows the intersection of significant structures with intense quadrants  $Q_j$ . The dashed lines are area fractions of the intersection of random  $Q_j$  structures with the same area as the significance structures. Figure 19(b) repeats the

## Causal features in turbulent channel flow

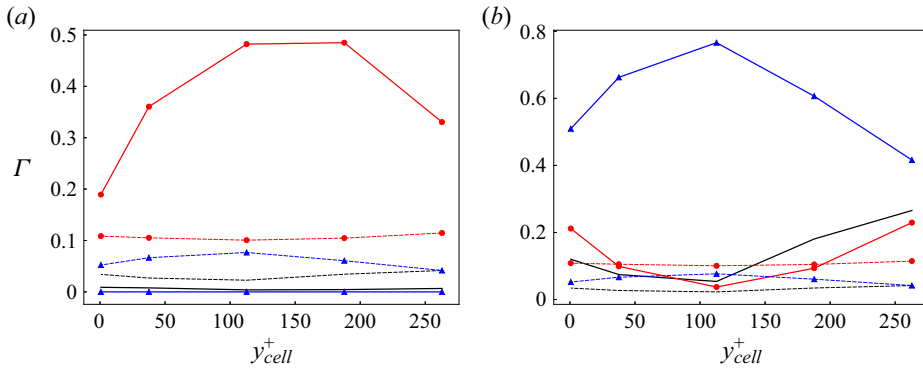


Figure 19. Area fraction of the significance structures intersected by intense quadrants, for  $t_{cell}^+ = 75$ . Red indicates  $Q_4$ ; blue indicates  $Q_2$ ; black indicates  $Q_1 \cup Q_3$ . Solid lines are conditioned to (a) significant, (b) irrelevant. Dashed lines are unconditional.

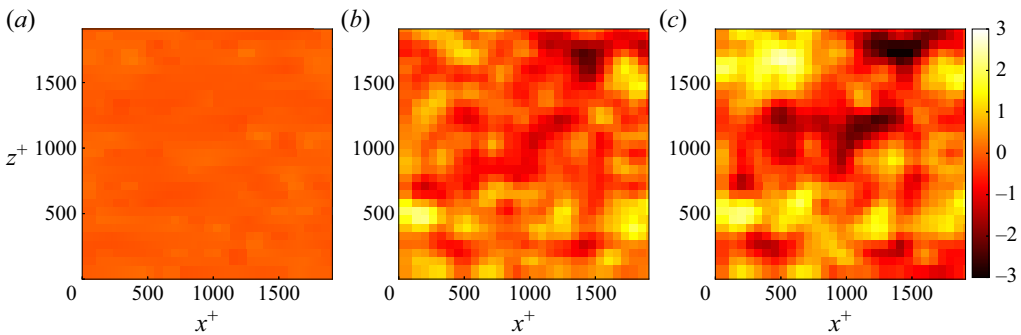


Figure 20. Heat maps of the relative significance  $\sigma_{ur}$  at various evaluation times. Note that the grid shows the position of the initial cells, whereas the colour indicates their relative significance evaluated at some future time. Here,  $t_{cell}^+ = 75$ ,  $y_{cell}^+ = 113$ . Evaluation times (a)  $0.01h/u_\tau$ , (b)  $0.14h/u_\tau$ , (c)  $0.28h/u_\tau \approx t_{sig}$ .

analysis for irrelevant. It is again clear that significant predominantly overlap  $Q_4$ , and irrelevant overlap  $Q_2$ , with a maximum at  $y^+ \approx 100-150$ .

The question of whether significant cells are organised into structures similar to those of intense quadrants is addressed in figure 20. Each heat map displays the same plane away from the wall. Cells are shown at their position at  $t = 0$ , but labelled by their relative significance evaluated some time after they are perturbed. The evaluation time increases from left to right. The heat map in figure 20(a) is featureless, reflecting the difficulty discussed in § 3 of predicting the future significance of a cell from its growth at short times. The organisation increases in figure 20(b), and is best developed in figure 20(c), where significance is evaluated at the optimum classification time  $t_{sig}$ . The size and organisation of the significance in figure 20(c) are very similar to those in the velocity maps in figures 14(a,b), with structures of  $O(h)$  organised into longer streaky structures.

This suggests the possibility that irrelevant and significant are essentially the same as sweeps and ejections. To test this hypothesis, both sets of cells are collected into individual connected objects for which the product  $\langle u \rangle_c \langle v \rangle_c$ , or  $\sigma_{ur}$ , is above or below the threshold required to isolate the  $\phi\%$  area fraction of their wall-parallel plane, as in Lozano-Durán *et al.* (2012). It is known that the wall-attached sweeps and ejections of the pointwise velocity form spanwise pairs (Lozano-Durán *et al.* 2012). A similar analysis is done here

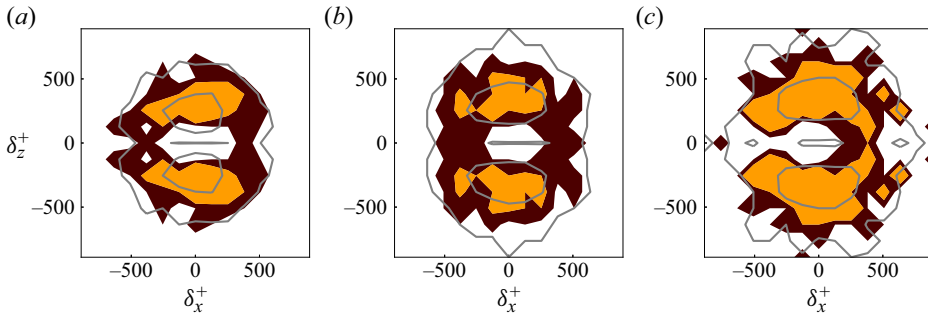


Figure 21. Joint probability density function of the relative position  $\{\delta_j\}$  of structures in close pairs. Filled contours are irrelevant–significant pairs, and lines are  $Q_2$ – $Q_4$ . Contours contain 60 % and 99 % of the data, and  $z$ -symmetry is enforced. Here, (a)  $y_{cell}^+ = 0$ , (b)  $y_{cell}^+ = 113$ , (c)  $y_{cell}^+ = 263$ . In all cases,  $l_{cell}^+ = 75$ .

for the cell-averaged quadrants and for the significance structures. The centroid of all the structures and their pairwise distance is computed first, and two structures, such as  $A_i$  and  $B_j$ , are defined as a pair if  $B_j$  is the closest object to  $A_i$ , and  $A_i$  is the closest object to  $B_j$ . It can be shown that the probability that significant and irrelevant structures are part of a close pair is similar to that for  $Q_2$  and  $Q_4$ , and much larger than for randomly located objects.

Figure 21 presents joint probability density functions of the relative positions of the nearest structures of similar kinds. Filled contours depict irrelevants around significant, and lines indicate ejections around sweeps. Both use spanwise symmetry to enhance statistical convergence, and it is clear that the pairs of the two types of structures have a similar organisation. Figure 22 shows the average spanwise width of the pairs as a function of wall distance and cell size. It is known from Lozano-Durán *et al.* (2012) that this width scales with  $y$  for attached  $Q_2$ – $Q_4$  pairs far from the wall. Our Reynolds number is too low for this self-similarity to hold, but figure 22 shows that, at least for the two smallest cell sizes, the width of the significance pairs grows with the distance from the wall, and approximately follows that of the quadrants. It is difficult to make an exact correspondence between single planes and slabs of relatively large cells, and the green line in the figure is probably a reflection of this difficulty. Its cell size,  $l_{cell}^+ = 150$ , is of the same order as the distance from the wall. Similarly, the apparently large discrepancy of the  $l_{cell}^+ = 75$  red line with the quadrant pairs at  $y_{cell} = 0$  is put in perspective by figure 21(a), which represents the same data.

Finally, figure 23 shows the relative positions of intense quadrants with respect to significance structures. Figure 23(a) is centred on significant, and shows that the closest sweep coincides with the significant structure, while the closest ejection avoids it. Figure 23(b), which is centred on irrelevants, shows that the opposite is true for them.

In summary, the results in this section show that highly significant and irrelevant structures respectively coincide with intense ejections and sweeps, at least statistically. They are organised in a similar way, and they most probably refer to the same structures, although it should be emphasised that this does not imply that all significance structures are intense quadrants, or vice versa.

## 6. Discussion and conclusions

We have analysed the causal relevance of flow conditions in wall-bounded turbulence, using ensembles of interventional experiments in which the effect of locally perturbing the

Causal features in turbulent channel flow

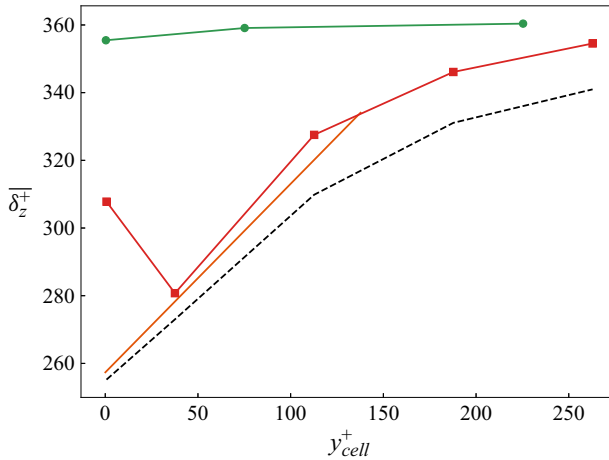


Figure 22. Mean spanwise distance among nearest significance or quadrant structures. Lines with symbols are significant–irrelevant pairs, with symbols denoting  $l_{cell}$ , as in table 2. The dashed line is  $Q_2$ – $Q_4$ .

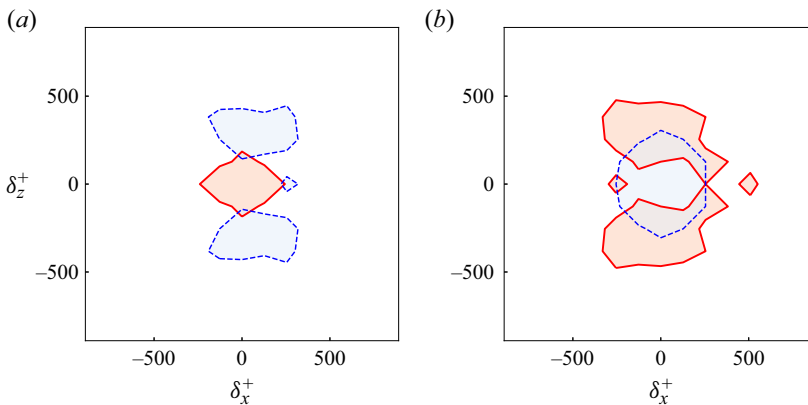


Figure 23. Joint probability density function of the relative position of closest structures of different types: (a) quadrants around significant; (b) quadrants around irrelevant. Red indicates nearest  $Q_4$ ; blue indicates nearest  $Q_2$ . Contours contain 60 % of data. Here,  $y_{cell}^+ = 113$ ,  $l_{cell}^+ = 75$ .

flow in a small cell is monitored at some future time. We have shown that the evolution of the kinetic energy of the perturbation velocity is mostly determined by its initial intensity, but that when the effect is characterised by the relative amplification of the perturbation energy, causality depends on the cell size, on the flow condition within the cell, and on its distance from the wall. It is then possible to enquire which properties of the flow at the time of the initial perturbation determine causality, and in this way, use the causality experiments as probes of the flow dynamics, rather than simply as a reflection of the dynamics of the perturbations (Jiménez 2020b; Encinar & Jiménez 2023).

We have shown that there is an optimum time at which causality can be measured most effectively, because the influence of different cell conditions is most pronounced. This time is proportional to the distance from the wall of the original intervention, and we have related it to the mean shear that the perturbation experiences as it evolves. When time is normalised with this shear, the evolution of perturbation applied to causally significant and to causally irrelevant cells collapses reasonably well (figure 17).

For perturbations away from the wall, the variables that predominantly determine causality are the streamwise and wall-normal velocities within the cell,  $\langle u \rangle_c$  and  $\langle v \rangle_c$ , with the latter becoming more influential farther from the wall. For wall-attached perturbations, the dominant variable is the local cell-averaged wall shear. Positive  $\langle u \rangle_c$ , negative  $\langle v \rangle_c$  and high wall shear are associated with high causality, and negative  $\langle u \rangle_c$ , positive  $\langle v \rangle_c$  and low shear are associated with irrelevance. This, together with the shear scaling mentioned above, suggests that wall-detached significant cells are predominantly associated with sweeps that carry the perturbation towards the stronger shear near the wall, whereas irrelevant ones are associated with ejections that carry it towards the weaker shear in the outer layers. This is confirmed by the conditional flow fields in figures 13–15, and by the quadrant analysis in figures 18 and 19.

We have also shown that causally significant and irrelevant cells are themselves organised into structures that share many characteristics of classical sweeps and ejections. For example, the latter are known to be organised in spanwise pairs, and we have shown that the same is true of causally significant and irrelevant structures. The dimensions of the two types of pairs are similar, and their relative positions are consistent with the identification of sweeps with significant cells and of ejections with irrelevant cells (figure 23).

However, as already noted at the end of § 5.2, not all sweeps and ejections are causally significant or irrelevant. Figures 13 and 14 show that as the perturbation experiments are performed closer to the wall, significant cells move towards the downstream end of the sweep, while irrelevant ones drift towards an interface between the ejection and a sweep downstream and underneath it. At the wall, this is consistent with a causally significant configuration in which a high-speed streak overtakes a low-speed one, and with a causally irrelevant situation in which the two streaks pull apart. In fact,  $\langle \partial_z w \rangle_c$  and  $\langle \partial_x u \rangle_c$  are among the leading indicators of causality for some wall-attached perturbations (figure 10).

This raises the question of how two structures that form a close pair can lead to different outcomes. A similar question was raised by Lozano-Durán & Jiménez (2014b) when they found that the vertical advection velocities of the sweep and ejection components of attached pairs are  $-u_\tau$  and  $+u_\tau$ , respectively. During the lifetime of the pair, this leads to relative vertical displacements of the order of the height of the pair, and to its dissolution. The answer offered at the time was that this was the mechanism that limits the lifetime of the pair, and a similar answer may apply here, since one of the results of this paper is that causality can be traced only to the moment when significant perturbations reach the wall. In fact, sweep–ejection pairs are known to be located at the interface between high- and low-velocity streaks (Lozano-Durán *et al.* 2012), and it is easy to see that their effect on the streamwise velocity would be to deform the streaks into meandering. Although the statistical confirmation of this model is beyond the scope of the data used in the present paper, figure 14 strongly suggests that the association of causality at the wall with the streamwise variation of  $\langle u \rangle_c$  refers to the leading and trailing edges of a streak meander. The causal significance of the off-wall sweeps would then reduce to their role in modifying the active downstream edge of the meander.

From an application perspective, the results of this study suggest new possibilities for turbulence control. This is not the place to discuss in detail the implementation of control strategies, but most current research centres on wall-attached sensors and actuators, while some of the results above suggest that if the focus is on altering the overall state of the flow, then it may be more efficient to act on motions detached from the wall and moving towards it. This is not a completely new subject. It is known that numerically manipulating the mean velocity profile in a channel appreciably modifies turbulence (Tuerke & Jiménez 2013), and it has been shown recently that a similar approach can fully relaminarise



the metastable turbulence in a circular pipe (Kühnen *et al.* 2018). While the technical challenges associated with manipulating the flow in the far field are clear, this approach is intriguing because it is not currently receiving much attention, and one cannot avoid being reminded of large-eddy breakup devices (LEBUs) (Alfredsson & Örlu 2018). These are typically passive devices that perturb the flow in all circumstances, and often result in a higher parasitic drag than what they save, but the above identification of locally causal and irrelevant flow regions suggests that it might be possible to design ‘smart’ LEBUs that act on the flow only ‘when useful’.

As for further work, several avenues should be explored, although most would require substantially more data and processing than the ones used here. For example, statistical confirmation of the continuity model outlined above should probably be done on computational boxes larger than the present one, to avoid artefacts on the behaviour of streaks. The same can be said about different Reynolds numbers. Similarly, the characterisation of causality by the integrated perturbation energy over the whole domain could probably be gainfully substituted by more specific measures, such as the energy of a particular layer, near or far from the wall, or by more practical ones, such as the skin friction. This would make the results more relevant to control, and probably illuminate flow interactions that are relevant to its physical understanding (e.g. small near-wall scales with large far-wall ones). Unfortunately, studies such as the present one involve large amounts of data that cannot be fully stored for re-processing. Much of the analysis is done ‘on the fly’ while the experiments are being carried out, and applying a new processing strategy involves a new set of simulations. On the other hand, prospective studies such as the present one are crucial to the design of any such future extension.

**Funding.** This work was supported by the European Research Council under the Caust Grant ERC-AdG-101018287.

**Declaration of interests.** The authors report no conflict of interest.

**Author ORCIDs.**

 Kosuke Osawa <https://orcid.org/0000-0001-6535-6241>;

 Javier Jiménez <https://orcid.org/0000-0003-0755-843X>.

**Appendix A. The perturbation evolution equation**

Consider a generic quantity  $T$  with source  $S$ , advected by a velocity field  $u_i$ ,

$$\partial_t T = -u_j \partial_j T + S, \tag{A1}$$

where repeated indices imply summation, and two independent experiments ‘ $a$ ’ and ‘ $b$ ’, denoted by superscripts of the respective fields. Consider now the evolution equation for the difference between the experiments. Define

$$\hat{g} = g^a - g^b, \tag{A2}$$

$$\bar{g} = (g^a + g^b)/2, \tag{A3}$$

for any  $g$ . Particularising (A1) for  $T^a$  and  $T^b$ , and subtracting one from the other, gives

$$\partial_t \hat{T} = -u_j^a \partial_j T^a + u_j^b \partial_j T^b + \hat{S}, \tag{A4}$$

which, since

$$\begin{aligned} \hat{u}_j \partial_j \bar{T} + \bar{u}_j \partial_j \hat{T} &= (u_j^a - u_j^b) \partial_j (T^a + T^b)/2 (u_j^a + u_j^b) \partial_j (T^a - T^b)/2 \\ &= u_j^a \partial_j T^a/2 - u_j^b \partial_j T^b/2 + u_j^a \partial_j T^b/2 - u_j^b \partial_j T^a/2 \\ &\quad + u_j^a \partial_j T^a/2 - u_j^b \partial_j T^b/2 - u_j^a \partial_j T^b/2 + u_j^b \partial_j T^a/2 \\ &= u_j^a \partial_j T^a - u_j^b \partial_j T^b, \end{aligned} \tag{A5}$$

can be written as

$$\partial_i \hat{T} = -\hat{u}_j \partial_j \bar{T} - \bar{u}_j \partial_j \hat{T} + \hat{S}. \tag{A6}$$

Multiplying (A6) by  $\hat{T}$ , we obtain

$$\begin{aligned} \partial_i \hat{T}^2 &= -2\hat{u}_j \hat{T} \partial_j \bar{T} - 2\bar{u}_j \hat{T} \partial_j \hat{T} + 2\hat{T} \hat{S} \\ &= -2\hat{u}_j \hat{T} \partial_j \bar{T} - \bar{u}_j \partial_j \hat{T}^2 + 2\hat{T} \hat{S}. \end{aligned} \tag{A7}$$

The evolution of the velocity perturbation magnitude follows from substituting  $u_i$  for  $T$  in (A7). The source of the evolution equation for  $u_i$  is  $S_i = -\partial_i p + \nu \partial_j^2 u_i$ , so that  $\hat{S}_i = -\partial_i \hat{p} + \nu \partial_j^2 \hat{u}_i$ , and

$$\begin{aligned} \partial_i \hat{u}_i^2 &= -2\hat{u}_i \hat{u}_j \partial_j \bar{u}_i - \bar{u}_j \partial_j \hat{u}_i^2 - 2\hat{u}_i \partial_i \hat{p} + 2\nu \hat{u}_i \partial_j^2 \hat{u}_i \\ &= -2\hat{u}_i \hat{u}_j \partial_j \bar{u}_i - \bar{u}_j \partial_j \hat{u}_i^2 - 2\partial_i(\hat{u}_i \hat{p}) + 2\nu \partial_j(\hat{u}_i \partial_j \hat{u}_i) - 2\nu(\partial_j \hat{u}_i)^2 \\ &= -2\hat{u}_i \hat{u}_j \partial_j \bar{u}_i - \partial_j\{\bar{u}_j \hat{u}_i^2 + 2\hat{u}_i \hat{p} \delta_{ij} - \nu \partial_j \hat{u}_i^2\} - 2\nu(\partial_j \hat{u}_i)^2 \\ &= P_{\varepsilon u} + C_{\varepsilon u} + D_{\varepsilon u}, \end{aligned} \tag{A8}$$

where  $\delta_{ij}$  is Kronecker's delta. The first and last terms in (A8) represent the production and dissipation of the perturbation energy, respectively. Note that velocity gradient in the production term is the average of two independent fields, and does not necessarily agree with the usual ensemble-averaged gradient. The terms in curly brackets are fluxes that do not contribute to  $\varepsilon_u$  when (A8) is integrated over the whole computational box. From left to right, they represent convection, pressure-strain and viscous diffusion, respectively. It is noteworthy that swapping  $a$  and  $b$  does not change (A8), in agreement with the symmetric way in which they are defined. In fact, (A8) is similar to the evolution equation for the structure function between the velocities at two neighbouring points, with the difference that there are no interactions here between the fields  $a$  and  $b$ .

#### REFERENCES

- ABE, H., ANTONIA, R. & TOH, S. 2018 Large-scale structures in a turbulent channel flow with a minimal streamwise flow unit. *J. Fluid Mech.* **850**, 733–768.
- DEL ÁLAMO, J.C. & JIMÉNEZ, J. 2003 Spectra of very large anisotropic scales in turbulent channels. *Phys. Fluids* **15**, L41–L44.
- ALFREDSSON, P.H. & ÖRLU, R. 2018 Large-Eddy BreakUp devices – a 40 years perspective from a Stockholm horizon. *Flow Turbul. Combust.* **100**, 877–888.
- ANGRIST, J.D., IMBENS, G.W. & RUBIN, D.B. 1996 Identification of causal effects using instrumental variables. *J. Am. Stat. Assoc.* **91**, 444–455.
- BRUNTON, S.L., NOACK, B.R. & KOUMOUTSAKOS, P. 2020 Machine learning for fluid mechanics. *Annu. Rev. Fluid Mech.* **52**, 477–508.
- CHERUBINI, S., ROBINET, J.-C., BOTTARO, A. & DE PALMA, P. 2010 Optimal wave packets in a boundary layer and initial phases of a turbulent spot. *J. Fluid Mech.* **656**, 231–259.

- CIOLA, N., DE PALMA, P., ROBINET, J.-C. & CHERUBINI, S. 2023 Nonlinear optimal perturbation of turbulent channel flow as a precursor of extreme events. *J. Fluid Mech.* **970**, A6.
- CRISTIANINI, N. & SHAWE-TAYLOR, J. 2000 *An Introduction to Support Vector Machines and Other Kernel-based Learning Methods*. Cambridge University Press.
- ENCINAR, M.P. & JIMÉNEZ, J. 2023 Identifying causally significant features in three-dimensional isotropic turbulence. *J. Fluid Mech.* **965**, A20.
- FARANO, M., CHERUBINI, S., ROBINET, J.-C. & DE PALMA, P. 2017 Optimal bursts in turbulent channel flow. *J. Fluid Mech.* **817**, 35–60.
- FERNEX, D., NOACK, B.R. & SEMAAN, R. 2021 Cluster-based network modeling – from snapshots to complex dynamical systems. *Sci. Adv.* **7**, eabf5006.
- FROYLAND, G. & PADBERG, K. 2009 Almost-invariant sets and invariant manifolds – connecting probabilistic and geometric descriptions of coherent structures in flows. *Physica D* **238**, 1507–1523.
- GRANGER, C.W.J. 1969 Investigating causal relations by econometric models and cross-spectral methods. *Econometrica* **37**, 424–438.
- HAMILTON, J.M., KIM, J. & WALEFFE, F. 1995 Regeneration mechanisms of near-wall turbulence structures. *J. Fluid Mech.* **287**, 317–348.
- HOYAS, S. & JIMÉNEZ, J. 2006 Scaling of the velocity fluctuations in turbulent channels up to  $Re_\tau = 2003$ . *Phys. Fluids* **18**, 011702.
- JIMÉNEZ, J. 2013 How linear is wall-bounded turbulence? *Phys. Fluids* **25**, 110814.
- JIMÉNEZ, J. 2018a Coherent structures in wall-bounded turbulence. *J. Fluid Mech.* **842**, P1.
- JIMÉNEZ, J. 2018b Machine-aided turbulence theory. *J. Fluid Mech.* **854**, R1.
- JIMÉNEZ, J. 2020a Dipoles and streams in two-dimensional turbulence. *J. Fluid Mech.* **904**, A39.
- JIMÉNEZ, J. 2020b Monte Carlo science. *J. Turbul.* **21** (9–10), 544–566.
- JIMÉNEZ, J. 2021 Collective organization and screening in two-dimensional turbulence. *Phys. Rev. Fluids* **6**, 084601.
- JIMÉNEZ, J. 2022 The streaks of wall-bounded turbulence need not be long. *J. Fluid Mech.* **945**, R3.
- JIMÉNEZ, J. 2023 A Perron–Frobenius analysis of wall-bounded turbulence. *J. Fluid Mech.* **968**, A10.
- JIMÉNEZ, J., DEL ÁLAMO, J.C. & FLORES, O. 2004 The large-scale dynamics of near-wall turbulence. *J. Fluid Mech.* **505**, 179–199.
- JIMÉNEZ, J. & KAWAHARA, G. 2013 Dynamics of wall-bounded turbulence. In *Ten Chapters in Turbulence* (ed. P.A. Davidson, Y. Kaneda & K.R. Sreenivasan), pp. 221–268. Cambridge University Press.
- JIMÉNEZ, J. & MOIN, P. 1991 The minimal flow unit in near-wall turbulence. *J. Fluid Mech.* **225**, 213–240.
- JIMÉNEZ, J. & PINELLI, A. 1999 The autonomous cycle of near-wall turbulence. *J. Fluid Mech.* **389**, 335–359.
- KAISER, E., NOACK, B.R., CORDIER, L., SPOHN, A., SEGOND, M., ABEL, M., DAVILLER, G., OSTH, J., KRAJNOVIĆ, S. & NIVEN, R.K. 2014 Cluster-based reduced-order modelling of a mixing layer. *J. Fluid Mech.* **754**, 365–414.
- KEEFE, L., MOIN, P. & KIM, J. 1992 The dimension of attractors underlying periodic turbulent Poiseuille flow. *J. Fluid Mech.* **242**, 1–29.
- KIM, H.T., KLINE, S.J. & REYNOLDS, W.C. 1971 The production of turbulence near a smooth wall in a turbulent boundary layer. *J. Fluid Mech.* **50**, 133–160.
- KIM, J., MOIN, P. & MOSER, R.D. 1987 Turbulence statistics in fully developed channel flow at low Reynolds number. *J. Fluid Mech.* **177**, 133–166.
- KOLMOGOROV, A.N. 1941 The local structure of turbulence in incompressible viscous fluids at very large Reynolds numbers. *Dokl. Akad. Nauk. SSSR* **30**, 301–305.
- KROGSTAD, P.-A., KASPERSEN, J.H. & RIMESTAD, S. 1998 Convection velocities in a turbulent boundary layer. *Phys. Fluids* **10**, 949–957.
- KÜHNEN, J., SONG, B., SCARSELLI, D., BUDANUR, N.B., RIEDL, M., WILLIS, A., AVILA, M. & HOF, B. 2018 Destabilizing turbulence in pipe flow. *Nat. Phys.* **14**, 386–390.
- LOZANO-DURÁN, A. & ARRANZ, G. 2022 Information-theoretic formulation of dynamical systems: causality, modeling, and control. *Phys. Rev. Res.* **4**, 023195.
- LOZANO-DURÁN, A., BAE, H.J. & ENCINAR, M.P. 2020 Causality of energy-containing eddies in wall turbulence. *J. Fluid Mech.* **882**, A2.
- LOZANO-DURÁN, A., FLORES, O. & JIMÉNEZ, J. 2012 The three-dimensional structure of momentum transfer in turbulent channels. *J. Fluid Mech.* **694**, 100–130.
- LOZANO-DURÁN, A. & JIMÉNEZ, J. 2014a Effect of the computational domain on direct simulations of turbulent channels up to  $Re_\tau = 4200$ . *Phys. Fluids* **26**, 011702.
- LOZANO-DURÁN, A. & JIMÉNEZ, J. 2014b Time-resolved evolution of coherent structures in turbulent channels: characterization of eddies and cascades. *J. Fluid Mech.* **759**, 432–471.

- LU, S.S. & WILLMARTH, W.W. 1973 Measurements of the structure of the Reynolds stress in a turbulent boundary layer. *J. Fluid Mech.* **60**, 481–511.
- NIKITIN, N. 2008 On the rate of spatial predictability in near-wall turbulence. *J. Fluid Mech.* **614**, 495–507.
- NIKITIN, N. 2018 Characteristics of the leading Lyapunov vector in a turbulent channel flow. *J. Fluid Mech.* **849**, 942–967.
- ORR, W.M.F. 1907 The stability or instability of the steady motions of a perfect liquid, and of a viscous liquid. Part I. A perfect liquid. *Proc. R. Irish Acad. A* **27**, 9–68.
- PEARL, J. 2009 Causal inference in statistics: an overview. *Stat. Surv.* **3**, 95–146.
- PEDREGOSA, F., *et al.* 2011 Scikit-learn: machine learning in Python. *J. Machine Learning Res.* **12**, 2825–2830.
- PEROT, B. & MOIN, P. 1995 Shear-free turbulent boundary layers. Part 1. Physical insights into near-wall turbulence. *J. Fluid Mech.* **295**, 199–227.
- PIROZZOLI, S. 2023 Searching for the log law in open channel flow. *J. Fluid Mech.* **971**, A15.
- RODWELL, M.J. & WERNLI, H. 2023 Uncertainty growth and forecast reliability during extratropical cyclogenesis. *Weath. Clim. Dyn.* **4**, 591–615.
- SCHMID, P.J., GARCÍA-GUTIÉRREZ, A. & JIMÉNEZ, J. 2018 Description and detection of burst events in turbulent flows. *J. Phys.: Conf. Ser.* **1001**, 012015.
- SOUZA, A.N. 2023 Transforming butterflies into graphs: statistics of chaotic and turbulent systems. [arXiv:2304.03362](https://arxiv.org/abs/2304.03362).
- SPALART, P.R., MOSER, R.D. & ROGERS, M.M. 1991 Spectral method for the Navier–Stokes equations with one infinite and two periodic dimensions. *J. Comput. Phys.* **96**, 297–324.
- TAIRA, K. & NAIR, A.G. 2022 Network-based analysis of fluid flows: progress and outlook. *Prog. Aerosp. Sci.* **131**, 100823.
- TANAHASHI, M., KANG, S.-J., MIYAMOTO, T., SHIOKAWA, S. & MIYAUCHI, T. 2004 Scaling law of fine scale eddies in turbulent channel flows up to  $Re_\tau = 800$ . *Intl J. Heat Fluid Flow* **25**, 331–340.
- TUERKE, F. & JIMÉNEZ, J. 2013 Simulations of turbulent channels with prescribed velocity profiles. *J. Fluid Mech.* **723**, 587–603.
- VELA-MARTÍN, A., ENCINAR, M.P., GARCÍA-GUTIÉRREZ, A. & JIMÉNEZ, J. 2021 A low-storage method consistent with second-order statistics for time-resolved databases of turbulent channel flow up to  $Re_\tau = 5300$ . *J. Comput. Sci.* **56**, 101476.
- VELA-MARTÍN, A. & JIMÉNEZ, J. 2021 Entropy, irreversibility and cascades in the inertial range of isotropic turbulence. *J. Fluid Mech.* **915**, A36.
- WALEFFE, F. 1997 On a self-sustaining process in shear flows. *Phys. Fluids* **9**, 883–900.
- WANG, M. & ZAKI, T.A. 2022 Synchronization of turbulence in channel flow. *J. Fluid Mech.* **943**, A4.
- YOSHIDA, K., YAMAGUCHI, J. & KANEDA, Y. 2005 Regeneration of small eddies by data assimilation in turbulence. *Phys. Rev. Lett.* **94**, 014501.